Optimal Multicompression Approach to Breast Elasticity Imaging

BY

Huini Du

B.E. (Shanghai Jiaotong University, China) 2002

Submitted in partial satisfaction of the requirements for the degree of

MASTER OF SCIENCE

in

Biomedical Engineering

in the

OFFICE OF GRADUATE STUDIES

of the

UNIVERSITY OF CALIFORNIA

DAVIS

Approved:

Michael F. Insana

Claire Pellot-Barakat

Simon R. Cherry

Committee in Charge

2004

TABLE OF CONTENTS

LIST OF FIGURES AND PHOTOGRAPHS

LIST OF TABLES

ABSTRACT

Breast lesion visibility in static strain imaging ultimately is noise limited. When correlation and related techniques are applied to estimate local displacements between two echo frames recorded before and after a deformation, target contrast increases linearly with the amount of deformation applied. However, above some deformation threshold, decorrelation noise increases more than contrast such that lesion visibility is severely reduced. Multicompression methods avoid this problem by accumulating displacements from many small deformations to provide the same net increase in lesion contrast as one large deformation but with minimal decorrelation noise. Unfortunately multicompression approaches accumulate echo noise (electronic and sampling) with each deformation step as contrast builds so that lesion visibility can again be reduced if the applied deformation increment is too small. This thesis uses signal models and analysis techniques to develop optimal multicompression strategies in the sense that strain image noise is minimized. The analysis predicts that displacement variance is minimal when the applied strain increment is between 0.003 and 0.004 in homogeneous media and 0.001 to 0.002 in highly heterogeneous media. Predictions are verified experimentally with gelatin phantoms and in vivo breast scans from patients with tumors.

1. INTRODUCTION

1.1. Concept of elastography

Physicians have used palpation to aid tumor detection for centuries. The increases in hardness of tissue, which indicate changes in elastic properties such as Young's modulus, is related to pathological process. For example, scirrhous carcinoma of the breast appears as extremely hard nodules, which are a result of increased stromal density. Pathologic fatty and/or collagenous deposits may also decrease/increase the tissue elasticity for some diseases. However, lesion detection by manual palpation is subjective, and often it is not possible to sense small lesions located deep inside the body. Nevertheless, palpation remains in use because differences in tissue elasticity can be an order of magnitude,[2,3] whereas bulk modulus variations in soft tissue, which is the primary contrast mechanism in current ultrasound imaging, are as small as only a few percent.[4] High object contrast makes tissue elasticity imaging a new and promising modality with significant diagnostic value. Elastography, as a rapidly developing diagnostic technique, gives qualitative and quantitative measurements for the tissue viscoelastic properties. Malignant lesions, which may appear as benign lesions in mammography and sonography, can now be differentiated based on their distinct viscoelastic properties.

Many elastographic techniques have been developed during the past two decades. Different modalities including ultrasound, nuclear magnetic resonance and computed tomography have been used in elastography. Ultrasound has major advantages com-

pared to other imaging modalities: it is inherently real-time, low cost and low risk. Since none of these modalities can directly image the fundamental tissue parameters, scientists have to reconstruct images displaying the tissue mechanical properties based on the information provided by these imaging techniques. Only ultrasound and MRI using phase sensitive detection, which increases their sensitivity for detecting small movements.

Different tissue stress excitations have been employed and different parameters of tissue motion have been extracted for elastography. In 1987 and 1988, Lerner and Parker reported ultrasonic measurements for imaging tissue stiffness. They termed their approach sonoelasticity. In their experiments, external mechanical stimulation of target tissues were applied and Doppler ultrasound was applied to detect displacement from relative tissue motion.[5] Yamakoshi et.al also applied low-frequency ultrasound from the surface of the sample to excite internal vibration. They mapped the amplitude and phase of the wave propagation inside tissue.[6] In 1991, Ophir et al. applied external static deformation to tissues and measured strain by assuming the medium was linear, isotopic and elastic. Ultrasound pre- and post-compression A-line data were collected for cross-correlation analysis.[7] The strain profile inside the tissue along the transducer axis was calculated. These various techniques for elastography can be divided into two groups based on the temporal characteristics of their excitation methods[8]: dynamic methods (Lerner and Parker, Yamakoshi et.al) and static methods (Ophir et.al). In static methods, the tissue is compressed slowly and the distribution of its displacement is measured. The measured distribution of

strain as derivative of displacement is related to the predicted distribution of stress and the resulting parameters of moduli are deduced through elasticity equations. On the other hand, dynamic methods rely on the shear wave equation, which is local in character with its differential form. Material properties such as the shear moduli can be derived from the displacement measured during shear wave propagation in tissue.

Recent researches demonstrate promising applications of elastography in medicine and biology. Patients experiments have shown the efficiency of elastography in identifying lesions in tissue and distinguishing benign from malignant masses.[9] A palpation imaging study including 29 patients shows significant changes in elasticity sequences for fibroadenoma, cysts and carcinomas.[10] B-mode ultrasound images and strain images for the same objects are displayed side by side. Benign lesions tend to have about the same size in both B-mode and elasticity images while carcinoma typically are 2 to 3 times larger in elasticity images than in B-scans, presumably because elasticity images are sensitive to the desmoplastic reaction surrounding most breast malignancies. Elastography is also of great interest for the diagnosis of vascular diseases. Diagnostically important feature of arterial walls can be non-invasively assessed by ultrasound.[11] Elastography can be combined with blood velocity (flow) images to describe temporal and spatial features of vascular mechanics for diagnosis of vascular disease.[12] Nightingale et.al have proposed the acoustic radiation force impulse (ARFI) imaging technique that can generate local movements and detect displacements of in vivo soft tissue on the order of $10\mu m$.[13] As a method of palpation by remote sensing, elastography is proving it can provide unique and important

diagnostic information.

We choose static compression method for elastography using the ultrasonic modality. To be temporally coherent, tissue motion must be confined to the image plane to avoid generating large errors (strain noise). We then scan the object using broad pulse-echo ultrasound. A radio-frequency(RF) echo field is recorded with high spatial resolution ($< 1mm$) at first. This pre-compression echo field is the reference for comparing the position of scatterers after compression. Next we compress the tissue, hold it and re-scan the tissue to record the position of displaced scatterers in the compressed state. A sequence of signal processing techniques including global, local companding[14] and cross-correlation estimation are used to measure the displacement occurring between the time that pre- and post- compression echo fields were recorded. The axial gradient of the displacement is computed to estimate internal strain tensor components.[15] The strain profile can then be converted to an elastic modulus profile.[7] Generally, in static methods, strain images are sufficient to assess tissue stiffness. The contrast of strain images is inversely proportional to the contrast of the Young's modulus distribution. Stiff regions of the tissue with high Young's modulus will have low strain and appear dark in the strain images; while soft regions with low Young's modulus will have high strain and appear as bright region in the strain image.

1.2. Elastic Breast Imaging

The efficiency of elastography in tumor detection has been shown in many studies as mentioned in the previous section. Accurate and early detection of breast cancer is expected to save many lives from a disease that affects 1 in 10 women[16] in the US. Breast cancer is the second leading cause of cancer death in women. Physicians use imaging to stage the disease and evaluate the extensiveness of the cancer and whether it has spread to lymph nodes or to other organs such as lung and liver. Breast cancer can be divided to five stages: stage 0 (carcinoma in situ) to IV. Some of the stages are further sub-divided using the letters A, B, and C. In general, the lower the number, the less the cancer has spread. Late stages indicate a more advanced and dangerous cancer. The American Cancer Society (ACS) has reported the 5-year survival rates (percentage of patients who live at least 5 years after their cancer is diagnosed) in different cancer stages as in Table 1.[16]

The ACS also predicts an increase in survival rate from 82% to 95% if all women are screened as recommended. Detecting the breast cancer in an early stage, before metastasis occur, can increase the survival rate and reduce cancer-related deaths. The severity of the breast cancer disease and the large population of patients prone to acquiring breast cancer make it an important application for elastography. Preliminary research achievements mentioned in the first section suggest that elastography is very promising in breast cancer detection.

Special characteristics need to be considered for breast elasticity imaging. In

Table 1. Breast Cancer Survival by Stage

Stage	5-year Survival Rate
0	100%
I	98%
IIA	88%
IIB	76%
IIIA	56%
IIIB	49%
IV	16%

breast imaging, compressive strains greater than 1% of the total tissue thickness are often applied to generate sufficient contrast resolution for lesion detection. Krouskop et.al found that the magnitude of elastic modulus of the glandular tissue increased by an order above the normal glandular tissue at high strain level.[3] Since the range of elastic modulus values in breast tissue is large, relatively large deformations are desired to ensure each region is strained to generate signals within the dynamic range of the technique. But the large heterogeneity of breast tissue stiffness can result in another problem for image quality. If we strain the stiffest tissues, e.g., tumors, the deformation to the surrounding regions made by the same compression can be quite high. The problem with large applied strain is that the RF echo signals from sequential echo frames can be highly decorrelated. Then when the correlation-based strain estimator is applied on the pre- and post-compression data, displacement errors

increase due to the echo decorrelation. The loss of inter-frame echo coherence, which generates decorrelation noise in strain images is the major source of strain imaging noise and the major cause of poor image quality. Fig.1 illustrates the effect of applied compression to the strain images of a phantom with a hard inclusion. The larger the applied strain, the higher the contrast. However the decorrelation noise also increases with the applied strain. This salt-and-pepper decorrelation noise can greatly reduce the image quality.

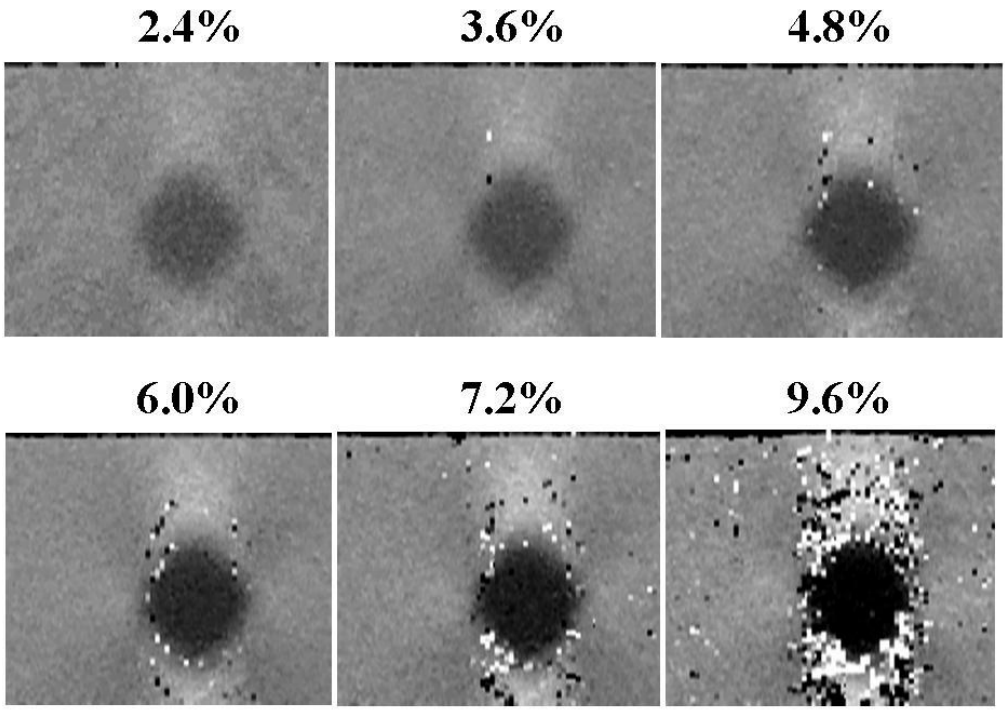

Figure 1. Strain images under different compression.

1.3. Multicompression approach

Multicompression is a technique that allows large deformation without incurring great decorrelation noise. It was first presented by O'Donnell's group.[17,18] In their papers, they pointed out that large internal displacements are desired to maximize the signal to noise ratio of displacement and strain estimates. But their speckle tracking method for displacements estimation failed in the limit of large displacements and strains. The reasons are that large displacements can move scatterers in and out of the plane of the imaging system; large strains change the spatial distribution of scatterers within an image area, thus decorrelating the speckle patterns used for motion tracking. To reduce decorrelation noise, they used multiple small step deformations that result in the same large total deformation. The total displacement was then calculated by accumulating the displacements between each small deformation. The accumulation of displacements from many small deformations can provide the necessary contrast resolution for large deformations, although the echo noise increments from each step eventually will accumulate to again decorrelate echo signals. Therefore the amount of compression applied per step that gives the best image quality is the optimization problem discussed in this thesis.

Multicompression has been studied previously but only empirically. Varghese and Ophir developed a general theoretical framework which they termed strain filter. They used the strain filter model for the description of the relationship between the resolution, dynamic range, sensitivity and elastographic SNR.[19] They combined the temporal stretching and multicompression averaging to improve the elastography

quality.[20] These two techniques were evaluated by comparing the elastographic SNR obtained for four different methods: (i) single compression without stretching; (ii) single compression with stretching; (iii) multicompression averaging without stretching and (iv) stretching-multicompression averaging. Their simulation showed that method (iv) can give the best image quality and largest elastographic SNR.

A German group has introduced a real-time strain imaging system using phase-root seeking algorithm for strain estimation. In their paper,[21] they qualitatively estimated the decorrelation noise proportional to the amount of applied strain and supposed a higher order dependency for higher strain. They studied the other types of noise from RF-echoes (electronic and acoustic noise etc.) and their simulation results showed negative covariance between frames. They indicated that by summing successive frames, the total deformation can be achieved while the electronic/acoustic noise will not overly increase. Consequently, they suggested choosing very high frame rate for multicompression for the purpose of decorrelation noise reduction.

All these studies show the benefit of the multicompression approach in elastography: great reduction of the decorrelation noise. Until now, there was no analytical methods for balancing decorrelation from large, complex motion with that from echo noise. The motivation of this thesis is to analyze all the noise sources of breast elasticity imaging and try to optimize the multicompression approach for the purpose of image quality improvement. To find the combination of system parameters that yields the smallest net noise, we are developing methods for predicting estimation errors from all major sources. Since the estimation bias is relatively small,[22] our focus is

on displacement variance. Variance bounds are predicted from knowledge of the echo *coherence function*.[23] Coherence functions can reveal how the physics of tissue deformation and associated measurement instrumentation determine displacement errors,[1] but only if the signal models accurately represent the echo data. In this thesis, a description of the waveform model for ultrasonic echo signals is first presented. Then deriving from the model, the maximum-likelihood estimator is used with the coherence function to predict the Cramér-Rao lower bound for displacement variance. The variance bound is the criteria for optimizing the design of multicompression strain imaging methods. Experimental data is collected to evaluate our analytical prediction. Finally, the application of multicompression approaches in clinical experiments is discussed.

2. THEORY IN CONTINUOUS DOMAIN

2.1. Ultrasonic waveform model

The following discussion through the end of Chapter 2 is a review of theory presented elsewhere.[1] The review sets the scene for my research.

2.1.1. Echo signal and coordinate transformation

Before introducing the waveform model, the definition of the ultrasonic echo signal and the coordinate transformation in continuous time domain will first be stated. For a linear, shift-invariant ultrasonic system with pulse-echo transfer function $\tilde{h}(\mathbf{x})$ in spatial domain, where $\mathbf{x} = (x_1, x_2, x_3)^t$ is a spatial variable denoting 3-D position, the echo signal can be expressed as the convolution of the scattering amplitude and transfer function. Let $z(\mathbf{x})$ stand for the specific acoustic impedance distribution which is an ergodic, zero-mean, Gaussian random process. The scattering amplitude is proportional to the second order derivative of $z(\mathbf{x})$. With the existence of a signal-independent noise process $n(\mathbf{x})$, the echo signal can be written as:

$$\begin{aligned} g(\mathbf{x}) &= \tilde{h}(\mathbf{x}) \otimes \frac{1}{2\pi z_0} \frac{\partial^2 z(\mathbf{x})}{\partial x_1^2} + n(\mathbf{x}) \\ &= \frac{1}{2\pi z_0} \int_{-\infty}^{\infty} d\mathbf{x}' \, \tilde{h}(\mathbf{x} - \mathbf{x}') \, \frac{\partial^2 z(\mathbf{x}')}{\partial x_1'^2} + n(\mathbf{x}) \\ &= [h \otimes z](\mathbf{x}) + n(\mathbf{x}). \end{aligned} \tag{1}$$

$h(\mathbf{x})$ is defined as the second order derivative of the ultrasonic system transfer function in Eq.2:

$$h(\mathbf{x}) = \frac{1}{2\pi z_0} \frac{\partial^2 \tilde{h}(\mathbf{x})}{\partial x_1'^2}. \tag{2}$$

From Eq.1 and 2, we can see that the echo signal is directly related to the impedance distribution.[24,25]

When a force is applied to the tissue in elastography, the object is deformed, and so are the axes of the coordinate system. The deformation of a large area can be segmented into small regions as shown in Fig.2.

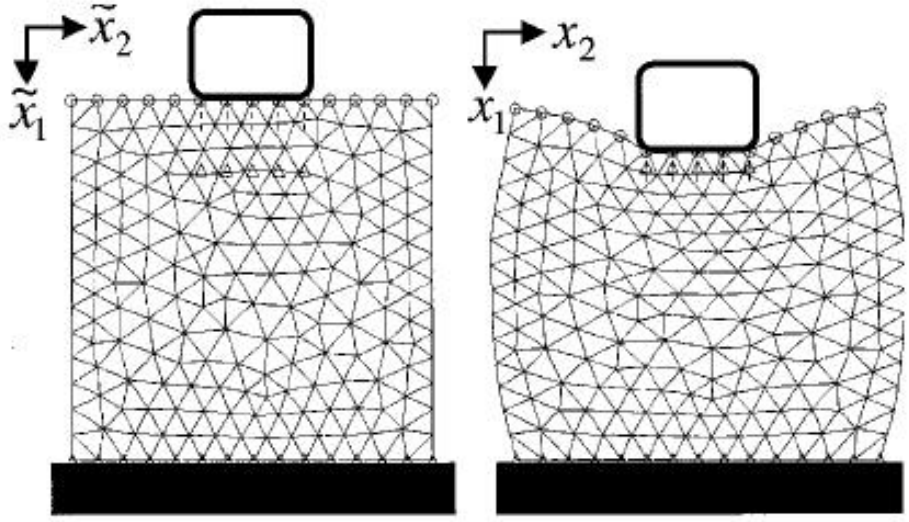

Figure 2. Deformation of an elastically uniform medium

All the later processing should be done in an identical coordinate space. It is necessary to express the coordinates of the impedance distribution before deformation, labeled $\tilde{\mathbf{x}}$, in terms of that after deformation, $\mathbf{x}$. We can map $\mathbf{x}$ in terms of $\tilde{\mathbf{x}}$ by a linear transformation matrix $\mathbf{A}$ and a translation vector $\mathbf{a}$:

$$\begin{aligned} \mathbf{x}(\tilde{\mathbf{x}}) &= \mathbf{A}\tilde{\mathbf{x}} + \mathbf{A}\mathbf{a} \\ \tilde{\mathbf{x}}(\mathbf{x}) &= \mathbf{A}^{-1}\mathbf{x} - \mathbf{a} \end{aligned} \tag{3}$$

A and **a** mathematically model the physical deformation applied to the object as an affine transformation of the coordinate systems.

2.1.2. Waveform warping

Chaturvedi et.al. developed *companding* methods as a technique for reducing decorrelation noise in strain estimates.[14] It is similar to waveform companding for time delay estimation in radar and sonar applications.[26] Companding conditions the echo data before cross-correlation techniques are applied to allow larger plane-strain deformation and hence large image contrast with minimum decorrelation. Displacement estimation using companding has three steps[14]:

1) The coarsest estimates of the displacement are used to measure the overall displacement and average strain in the plane applied to one frame with respect to another. Echo data in the pre-deformation frame are translated and scaled in two dimensions to mimic the physical deformation applied to the object image in the post-deformation frame. The process of detecting overall movement and then deforming echo signals to compensate is known as *global companding* compression and expanding echo signals.

2) 2-D displacements are measured at an intermediate-sized spatial resolution (several millimeters) and used to warp the echo signals now using a *local companding* process.

3) Finally displacements are measured at the highest spatial resolution by 1-D axial correlation of twice-companded echo frames.

The primary purpose of the first two companding steps is to maximize coherence between the pre- and post-compression waveforms to be cross correlated in the third step. Displacements measured at each stage of the process improve the condition of the data for displacement estimation at higher resolution. To include more general motions, such as shearing and rotation, the companding process can be generalized by *warping* the pre-compression signal field prior to cross correlation.[27] The process of warping can also be modeled as a linear transformation from the pre- to post-deformation coordinates:

$$\begin{aligned} \mathbf{x}(\tilde{\mathbf{x}}) &= \mathbf{B}\tilde{\mathbf{x}} + \mathbf{B}\mathbf{b} \\ \tilde{\mathbf{x}}(\mathbf{x}) &= \mathbf{B^{-1}}\mathbf{x} - \mathbf{b} \end{aligned} \tag{4}$$

According to Eq.1 the pre-compression echo signal can be written in terms of $\mathbf{x}$ as:

$$g(\mathbf{x})|_{t_0} = [h \otimes z](\mathbf{x}) + n(\mathbf{x}) \tag{5}$$

Applying Eq.4 to Eq.5, the warped pre-compression signal is :

$$\begin{aligned} g_0(\mathbf{x}) &= g(\mathbf{B^{-1}}\mathbf{x} - \mathbf{b})|_{t_0} \\ &= \left[\int_\Omega d\mathbf{x}'\ h(\mathbf{B^{-1}}\mathbf{x} - \mathbf{b} - \mathbf{x}')\ z(\mathbf{x}')\right] + n_0(\mathbf{B^{-1}}\mathbf{x} - \mathbf{b}) \end{aligned} \tag{6}$$

While the post-compression signal can be expressed as a physical deformation of the object scattering function:

$$\begin{aligned} g_1(\mathbf{x}) &= g(\mathbf{x})|_{t_1} \\ &= \left[\int_\Omega d\mathbf{x}' h(\mathbf{x} - \mathbf{x}') z(\mathbf{A^{-1}}\mathbf{x}' - \mathbf{a})\right] + n_1(\mathbf{x}) \end{aligned} \tag{7}$$

where t_0 and t_1 respectively denote the times of the pre- and post-compression echo data acquisitions. $n_0(\mathbf{u})$ and $n_1(\mathbf{u})$ are different realizations of signal-independent, white Gaussian noise processes. The matrix $\mathbf{A}$ and vector $\mathbf{a}$ describe the physical deformation of the impedance field coming from the static force applied to the object, while $\mathbf{B}$ and $\mathbf{b}$ model the signal processing procedure applied to the pre-compression field to mimic $\mathbf{A}$ and $\mathbf{a}$. These processors are illustrated in Figure 3 as the ultrasonic waveform model.[1] where $N_0(\mathbf{u})$, $N_1(\mathbf{u})$ and $H(\mathbf{u})$ are the Fourier transform of the

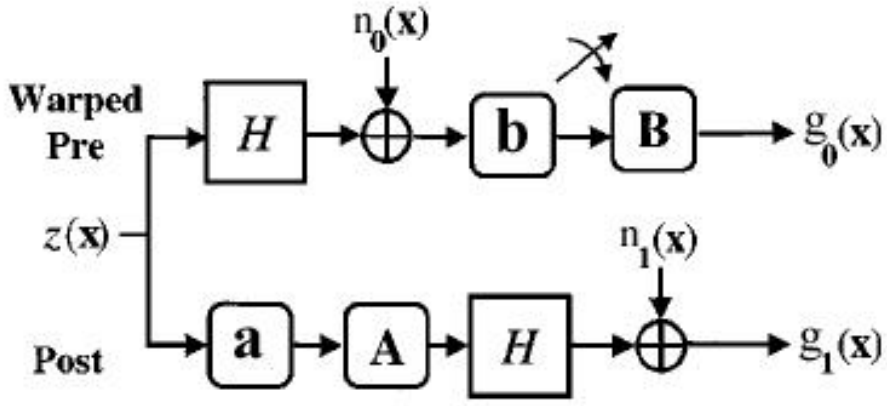

Figure 3. Ultrasonic waveform model

noise $n_0(\mathbf{x})$, $n_1(\mathbf{x})$ and of the point spread function of the imaging system $h(\mathbf{x})$.

2.2. Coherence function of strain imaging

A coherence function in the frequency domain is defined to describe the degree of spatial registration between the warped pre-compression and post-compression echo signals. Let $G_0(\mathbf{u})$, $G_1(\mathbf{u})$ be the spatial Fourier transform of $g_0(\mathbf{x})$ and $g_1(\mathbf{x})$. We

can define the complex coherence function $\gamma_{g_1g_2}(\mathbf{u})$ as the ratio of the cross power spectral density over the autospectral densities in Eq.8:

$$\gamma_{g_1g_2}(\mathbf{u}) = \frac{S_{g_0g_1}(\mathbf{u})}{\sqrt{S_{g_0g_0}(\mathbf{u})S_{g_1g_1}(\mathbf{u})}} = \frac{E\{G_0^*(\mathbf{u})G_1(\mathbf{u})\}}{\sqrt{E\{|G_0(\mathbf{u})|^2\}E\{|G_1(\mathbf{u})|^2\}}} \tag{8}$$

The absolute square of the complex coherence is the magnitude squared coherence (MSC) expressed in Eq.9:

$$|\gamma_{g_1g_2}(\mathbf{u})|^2 = \frac{E\{G_0^*(\mathbf{u})G_1(\mathbf{u})\}E\{G_0(\mathbf{u})G_1^*(\mathbf{u})\}}{E\{|G_0(\mathbf{u})|^2\}E\{|G_1(\mathbf{u})|^2\}} \tag{9}$$

The MSC function is a frequency-domain measurement of similarity for the two data sets. $E\{\cdot\}$ denotes the expectation and G^* is the complex conjugate of G. The range of MSC is: $0 \leq |\gamma_{g_1g_2}|^2 \leq 1$.[28] In situation where $|\gamma_{g_1g_2}|^2 \simeq 1$, warping was successful and the strain image will have little decorrelation noise. In practice, however, MSC>0.9 is acceptable.[1] We select the warping matrix $\mathbf{B}$ and vector $\mathbf{b}$ to maximize MSC.

Applying the Fourier scaling properties to Eq.6 and 7, the signal MSC function is found to be only depended on the object MSC function and the net signal-to-noise ratio (SNR)[1]:

$$|\gamma_{g_1g_2}(\mathbf{u})|^2 = \frac{|\gamma_{z_1z_2}(\mathbf{u})|^2 SNR(\mathbf{u})}{1 + SNR(\mathbf{u})}, \tag{10}$$

The coherence function is thus separable into factors related to the medium, $|\gamma_{z_1z_2}|^2$, and the imaging system and data processing steps via a net signal to noise ratio SNR. The MSC for the scattering medium is defined as:

$$|\gamma_{z_1z_2}(\mathbf{u})|^2 = \frac{E\left\{Z(\mathbf{A}^t\mathbf{u})Z^*(\mathbf{B}^t\mathbf{u})\right\}E\left\{Z^*(\mathbf{A}^t\mathbf{u})Z(\mathbf{B}^t\mathbf{u})\right\}}{E\left\{|Z(\mathbf{A}^t\mathbf{u})|^2\right\}E\left\{|Z(\mathbf{B}^t\mathbf{u})|^2\right\}} \tag{11}$$

where $Z(\mathbf{u})$ is the spatial Fourier transform of the scattering function $z(\mathbf{x})$. The net signal-to-noise ratio is

$$SNR(\mathbf{u}) = \frac{S/N_0(\mathbf{u})S/N_1(\mathbf{u})}{1 + S/N_0(\mathbf{u}) + S/N_1(\mathbf{u})} \tag{12}$$

with channel signal-to-noise ratios S/N_0 and S/N_1 corresponding to warped pre-compression field and post-compression field respectively:

$$\begin{aligned} S/N_0(\mathbf{u}) &= \frac{|H(\mathbf{B}^t\mathbf{u})|^2 E\left\{|Z(\mathbf{B}^t\mathbf{u})|^2\right\}}{E\left\{|N_0(\mathbf{B}^t\mathbf{u})|^2\right\}}, \\ S/N_1(\mathbf{u}) &= \frac{(\det \mathbf{A})^2|H(\mathbf{u})|^2 E\left\{|Z(\mathbf{A}^t\mathbf{u})|^2\right\}}{E\left\{|N_1(\mathbf{u})|^2\right\}} \end{aligned} \tag{13}$$

2.3. Maximum-likelihood (ML) strategy for displacement estimation

2.3.1. Cross Correlator estimator

After warping, cross correlation is applied to estimate residual displacement. The generalized cross correlator includes filtering with frequency response filter function $W(\mathbf{u})$ and is illustrated in Fig.4. This model was originally applied in time only to estimate time-delay in sonar and radar systems. It was adapted to 3-D spatial deformation and introduced in displacement estimation in elastography.[1] For the pre- and post-compression signals $g_0(\mathbf{x})$ and $g_1(\mathbf{x})$, the displacement can be estimated from the value of the delay at the peak of their cross correlation function[8]:

$$\begin{aligned} \hat{\tau} &= \arg\max_{\tau} \ \hat{R}_{g_0 g_1}(\tau) \\ &= \arg\max_{\tau} \int_{-\infty}^{\infty} d\mathbf{x}\ g_0(\mathbf{x}+\tau) g_1(\mathbf{x}) \end{aligned} \tag{14}$$

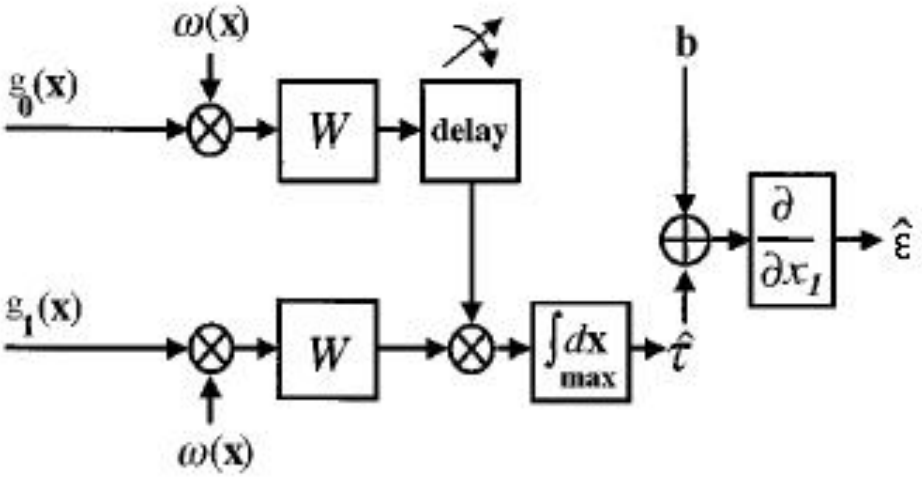

Figure 4. Generalized cross correlator and strain estimator.

The location of the peak of the integration gives the estimated displacement $\hat{\tau}$. In order to improve the accuracy of the delay estimation $\hat{\tau}$, it is desirable to prefilter $g_0(\mathbf{x})$ and $g_1(\mathbf{x})$ prior to the integration in Eq.14 and thereby weight spatial frequency component according to MSC function at that frequency.[29] The cross correlation between the signals can be related to the cross power spectral density function by Fourier transformation relationship:

$$\hat{R}_{g_0 g_1}(\tau) = \int_{-\infty}^{\infty} d\mathbf{u}\ \hat{S}_{g_0 g_1}(\mathbf{u}) e^{i2\pi \mathbf{u}\tau} \tag{15}$$

Suppose the filter function $\omega(\mathbf{x})$ is applied to each echo signal. Then the estimate of the cross correlation can be given by the integral:

$$\hat{R}_{g_0 g_1}(\tau) = \int_{-\infty}^{\infty} d\mathbf{u}\ W^2(\mathbf{u}) \hat{S}_{g_0 g_1}(\mathbf{u}) e^{i2\pi \mathbf{u}\tau} \tag{16}$$

This displacement estimation in acoustic strain imaging is consistent with the generalized cross correlator approach described by Knapp and Carter for 1-D time estimation if it is extended to higher spatial dimensions.[26]

For 1-D cross-correlation in elastography, the estimated axial strain is derived by the derivative of displacement along the axial direction.

$$\hat{\epsilon} = \frac{\partial \hat{\tau}_1}{\partial x_1}, \tag{17}$$

2.3.2. ML method for waveform model[1]

Next we study the log-likelihood of the data to obtain the maximum likelihood estimate. The ML strategy is often used in signal processing for parameter estimation. Details about the ML strategy are stated in Appendix A. The maximum-likelihood estimator selects displacement $\hat{\tau}$ that maximizes the likelihood function $p(\hat{\mathbf{G}}|\theta)$.[30,31] The vector θ denotes all the unknown parameters that effect the joint probability density function, including $\mathbf{A}$, $\mathbf{B}$, $\mathbf{a}$, $\mathbf{b}$ etc. $\hat{\mathbf{G}}$ is the estimated spectral density. $\hat{G}_0(\mathbf{u})$, $\hat{G}_1(\mathbf{u})$ are continuous functions of frequency. Their Fourier series with N finite frequency components are used for approximation: $\hat{\mathbf{G}} = (\hat{G}_0(\mathbf{u}_1), \hat{G}_1(\mathbf{u}_1), \hat{G}_0(\mathbf{u}_2), \hat{G}_1(\mathbf{u}_2), \cdots, \hat{G}_0(\mathbf{u}_N), \hat{G}_1(\mathbf{u}_N))^t$.[1] Since each component $\hat{G}_0(\mathbf{u}_k)$, $\hat{G}_1(\mathbf{u}_k)$ can be regarded as a Gaussian random variable, the likelihood function is also a Gaussian function in $2N$ dimensions:

$$p(\hat{\mathbf{G}}|\theta) = \frac{\Omega'^{4N}}{(2\pi)^{2N}\det(\mathbf{Q})} \exp\big(-\frac{\Omega'^2}{2}\hat{\mathbf{G}}^\dagger \mathbf{Q}^{-1}\hat{\mathbf{G}}\big) \tag{18}$$

where $\hat{\mathbf{G}}^\dagger$ is the conjugate transpose of $\hat{\mathbf{G}}$, $E\{\hat{\mathbf{G}}\} = 0$, and the spectral density matrix $\mathbf{Q}$ is defined as:

$$\mathbf{Q} = \Omega'^2 E\{\hat{\mathbf{G}}\hat{\mathbf{G}}^\dagger\} \tag{19}$$

Ω' defines the region of support for the Fourier series representation. Then, after some algebra and approximation, the log-likelihood function can be written as:

$$\ln p(\hat{\mathbf{G}}|\theta) \simeq \Omega' \int_{-\infty}^{\infty} d\mathbf{u}\; Re\left\{G_0^*(\mathbf{u})G_1(\mathbf{u})W^2(\mathbf{u}) \times e^{-i2\pi\mathbf{u}^t(\mathbf{Aa}-\mathbf{Bb})}\right\}. \tag{20}$$

where

$$W^2(\mathbf{u}) = \frac{|\gamma_{g_0g_1}(\mathbf{u})|}{\sqrt{S_{g_0g_0}(\mathbf{u})S_{g_1g_1}(\mathbf{u})}(1-|\gamma_{g_0g_1}(\mathbf{u})|)^2} \tag{21}$$

This shows us the form of the prefilter W that provides a ML estimate. Under certain conditions, the ML estimator is equivalent to other prefilters while it has practical significance related to coherence in delay estimation and special advantage in variance bound prediction.[29]

$G_0^*(\mathbf{u})G_1(\mathbf{u})$ can be seen as the estimated cross spectral density:

$$\begin{aligned} G_0^*(\mathbf{u})G_1(\mathbf{u}) &= \hat{S}_{g_0g_1}(\mathbf{u}) \\ &= |\hat{\gamma}_{g_gg_1}(\mathbf{u})|e^{i2\pi\mathbf{u}^2\hat{\tau}}\sqrt{S_{g_0g_0}(\mathbf{u})S_{g_1g_1}(\mathbf{u})} \end{aligned} \tag{22}$$

Substituing Eq.22 into Eq.20, and $S_{g_0g_1}(\mathbf{u}) = E\{\hat{S}_{g_0g_1}(\mathbf{u})\}$, then:

$$\ln p(\hat{\mathbf{G}}|\theta) \simeq \Omega' \int_{-\infty}^{\infty} d\mathbf{u}\; \frac{|\hat{\gamma}_{g_1g_2}(\mathbf{u})||\gamma_{g_1g_2}(\mathbf{u})|}{(1-|\gamma_{g_1g_2}(\mathbf{u})|^2)} \times Re\left\{e^{-i2\pi\mathbf{u}^t(\mathbf{Aa}-\mathbf{Bb}-\hat{\tau})}\right\}. \tag{23}$$

ML displacement estimates are those that satisfy $\partial \ln p(\hat{\mathbf{G}}|\theta)/\partial\hat{\tau} = 0$.

The ML filter emphasizes data at spatial frequencies where the MSC is large. In compressed breast tissue, the coherence function is high at low frequencies and falls

off quickly with frequency as strain is applied. When the electronic noise is large, the coherence function will decrease correspondingly across the whole spectrum.

2.4. Cramér-Rao variance lower bound

The theory of Cramér-Rao variance bound is expressed in Appendix B. By Eq. 48, the variance of the displacement along x_1 direction is bounded by:

$$\begin{aligned} var(\hat{\tau}_1) &\geq -E\left\{\frac{\partial^2 \ln p(\hat{\mathbf{G}}|\theta)}{\partial \tau_1^2}\right\} \\ &= \frac{A_{12}^2 Y_1 + A_{22}^2 Y_2}{(A_{11}A_{22} - A_{12}A_{21})^2 Y_1 Y_2}. \end{aligned} \tag{24}$$

Y_1, Y_2 are defined as:

$$\begin{aligned} Y_1 &= 2\Omega' \int_{-\infty}^{\infty} d\mathbf{u}\, (2\pi u_1)^2 \frac{|\gamma_{g_1 g_2}(\mathbf{u})|^2}{(1 - |\gamma_{g_1 g_2}(\mathbf{u})|^2)} \\ Y_2 &= 2\Omega' \int_{-\infty}^{\infty} d\mathbf{u}\, (2\pi u_2)^2 \frac{|\gamma_{g_1 g_2}(\mathbf{u})|^2}{(1 - |\gamma_{g_1 g_2}(\mathbf{u})|^2)} \end{aligned} \tag{25}$$

Notice that for practical strain imaging where the motion of the object is confined in two dimensions, coordinate $\mathbf{x}$ and $\tilde{\mathbf{x}}$ have two dimensions, so $\mathbf{A}$ is a 2×2 matrix and $\mathbf{a}$ is a 2×1 vector. For the special case of an incompressible medium deformed in two dimensions by a scaling transformation, the off-diagonal elements of $\mathbf{A}$ are zero. That is, $A_{11} = A_{22}^{-1}$, $A_{12} = A_{21} = 0$. So the variance bound can be written as:

$$\begin{aligned} var(\hat{\tau}_1) &\geq \frac{1}{A_{11}^2 Y_1} \\ &= \left(2\Omega' A_{11}^2 \int_0^{\infty} d\mathbf{u}\, (2\pi u_1)^2 \frac{|\gamma_{g_0 g_1}(\mathbf{u})|^2}{(1 - |\gamma_{g_0 g_1}(\mathbf{u})|^2)}\right)^{-1}. \end{aligned} \tag{26}$$

The same result was found by Knapp and Carter[29] for one-dimension time-delay estimation using ML estimator, which shows our general result reduces to theirs for the 1-D situation. Eq.26 shows that the variance bound is directly related to A_{11} which indicates the applied strain ϵ in axial direction with the relationship $A_{11} = 1-\epsilon$. Increasing the strain will decrease A_{11} and scales the variance. Decreasing MSC will also indirectly increase the variance. The integration means that coherence in all frequencies will contribute to the displacement noise bound. It is obvious to see that low strain and high coherence will yield the smallest errors in displacement estimation. Unfortunately, they also provide low contrast. In subsequent chapters, we will see that the variance bound of Eq.(26) can be approximately achieved experimentally. Therefore Eq.(26) can predict errors and thus may be used to design low noise, high contrast imaging strategies.

3. SIGNAL MODEL IN DISCRETE DOMAIN

As reviewed in the last chapter, previous works assumed linear, shift-invariant systems and all calculations were made in the continuous domain.[1] In practice, the echo signals are discrete functions of time and the point spread functions are shift varying functions of time and space. This chapter extends the previous work to include more realistic situations.

3.1. Echo signals

We modified the signal model by combining it with the feature of the discrete-time model proposed in by Zemp et.al[32] as following. $\mathbf{g}_j$ is an $M \times N$ matrix of RF data samples that defines the j-th recorded echo frame. The impulse response function of the linear ultrasonic system is accurately characterized as a shift-varying, spatiotemporal function written as $h(\mathbf{x}, \mathbf{t})$; while the object function describing the scattering magnitude $z_j(\mathbf{x})$ is spatially continuous in two dimensions. Each data sample $g_j[m, n]$ of the echo signal matrix $\mathbf{g}_j$ results from a linear transformation of the scattering function $z_j(\mathbf{x})$ through the linear system $h(\mathbf{x}, \mathbf{t})$[32]:

$$\mathbf{g}_j = \int_{-\infty}^{\infty} d\mathbf{x}\; h(\mathbf{x}, \mathbf{t})\; z_j(\mathbf{x}) + \mathbf{n}_j\; . \tag{27}$$

The signal-independent echo noise matrix $\mathbf{n}_j$ also has a size of $M \times N$. The vector $\mathbf{x} = (x_1, x_2)$ describes continuous 2-D spatial coordinates (axial and lateral). We only consider the echo confined in one plane. $\mathbf{t} = t[m, n]$ describes the analogous discrete temporal coordinates (range and cross range), where $0 \leq m \leq M$ and $0 \leq n \leq N$.

Data are recorded sequentially in time $t[m,n] = (m+nM)T$ where m is the fast-time index (range) and n is a slow-time index (cross range). T is the RF sampling interval, MT is the pulse repetition interval, and the product NMT is the frame interval. Linear transformations of these coordinate systems define spatial deformations of the scattering function and warping of echo signal time series as shown in Chapter 2.

Arbitrary deformations of continuous objects or sampled data can be modeled as a set of affine transformations of the coordinates $\mathbf{x}$ or $\mathbf{t}$ that are applied to segmented regions of the object, Ω_i.[1] We still use $\mathbf{A}$ and $\mathbf{a}$ to model the physical deformation and $\mathbf{B}$ and $\mathbf{b}$ to model the echo signal warping. Assume we record the echo frame j before object deformation, the frame $j+1$ after deformation, and then apply local companding to the j-th frame such that $\mathbf{b} \simeq \mathbf{a}$ and $\mathbf{B} \simeq \mathbf{A}$. For echo signals in the region $t[m,n] \in \Omega_i$, there will be $M'N'(M' \leq M, N' \leq N)$ companded pre-compression samples given by

$$\begin{aligned} \mathbf{g}_j &= \int_{-\infty}^{\infty} d\mathbf{x}\; h(\mathbf{x}, \mathbf{B}^{-1}\mathbf{K}^{-1}\mathbf{t} - \mathbf{b})\; z_j(\mathbf{x}) \\ &\quad . \qquad + \; n_j(\mathbf{B}^{-1}\mathbf{K}^{-1}\mathbf{t} - \mathbf{b}) \;, \quad \forall \; t[m,n] \in \Omega_i \;. \end{aligned} \tag{28}$$

Corresponding echo samples in the post-compression frame are given by

$$\mathbf{g}_{j+1} = \int_{-\infty}^{\infty} d\mathbf{x}\; h(\mathbf{x}, \mathbf{t})\; z_j(\mathbf{A}^{-1}\mathbf{x} - \mathbf{a}) + \mathbf{n}_{j+1} \;. \tag{29}$$

The matrix

$$\mathbf{K} = \begin{bmatrix} 2/c & 0 \\ 0 & MT/Y \end{bmatrix}$$

defines the space-time transformation $\mathbf{t} = \mathbf{K}\mathbf{x}$ and Y is the spatial increment along the cross range axis (transducer pitch). Eqs. (28) and (29) are more realistic than those reported in chapter 2 since they are sampled in time and include the spatially-varying spatiotemporal impulse response of the instrument.

3.2. Coherence function

Frequency domain is also sampled discretely. Let $G_j[k,\ell]$ and $G_{j+1}[k,\ell]$ be the 2D discrete Fourier transforms of echo signals $g_j[m,n]$ and $g_{j+1}[m,n]$. Details about the MSC functions have been described in chapter 2. Now all the functions are discrete functions of time or temporal frequency, which is more descriptive of experimental data than continuous form. The definition of the complex coherence function is:

$$\gamma_g[k,\ell] = \frac{E\{G_j^*[k,\ell]\, G_{j+1}[k,\ell]\}}{\sqrt{E\{|G_j[k,\ell]|^2\}E\{|G_{j+1}[k,\ell]|^2\}}} \,. \tag{30}$$

The relationship between the signal MSC, the scattering MSC, and the net signal-to-noise ratio (SNR) is:

$$|\gamma_g[k,\ell]|^2 = \frac{|\gamma_z[k,\ell]|^2 \mathrm{SNR}[k,\ell]}{1+\mathrm{SNR}[k,\ell]} \,. \tag{31}$$

SNR is a function of the channel signal to noise ratios S/N_j and S/N_{j+1} for the warped pre- and post-compression echo waveforms, respectively,

$$\mathrm{SNR}[k,\ell] = \frac{S/N_j[k,\ell]\, S/N_{j+1}[k,\ell]}{1+S/N_j[k,\ell]+S/N_{j+1}[k,\ell]} \,. \tag{32}$$

3.3. Variance bound

The main advantage of the MSC function is its relationship to the Cramér-Rao lower bound of displacement variance.[29] For uniaxial compression of a 2-D incompress-

ible medium that generates strain ϵ, the lower bound on variance for displacements estimated along the beam axis, τ, is given by[1]

$$\mathrm{var}(\tau) \geq \frac{(cM'T)^2}{32\pi^2(1-\epsilon)^2}\left(\sum_{k,\ell\in\Omega_i} k^2 \frac{|\gamma_g[k,\ell]|^2}{1-|\gamma_g[k,\ell]|^2}\right)^{-1} , \tag{33}$$

where c is the longitudinal sound speed and it is assumed that $E\{\tau\} = 0$.

The derivation of strain from displacement is stated in Eq.17. In practice, the strain is estimated from the difference equation:

$$\hat{\epsilon} = \frac{\tau^1 - \tau^2}{\Delta X} \tag{34}$$

where ΔX is the strain pixel size. The superscript numbers label the positions of two displacement estimates from adjacent waveform segments along the beam. The strain variance is approximated from displacement variance by propagation of error,[33]

$$\begin{aligned} \mathrm{var}(\epsilon) &= \frac{\mathrm{var}(\tau^1) + \mathrm{var}(\tau^2) - 2\mathrm{cov}(\tau^1,\tau^2)}{\Delta X^2} \\ &\simeq \frac{2\mathrm{var}(\tau)}{X\Delta X} . \end{aligned} \tag{35}$$

X is the correlation window length. Both parameters are measured in units of length.

4. METHODS

4.1. Controlled phantom deformation.

Experimental data were acquired from a 5-cm cubic block of gelatin in which fine graphite scattering particles were randomly suspended.[34] The gelatin block was compressed uniformly from above by a transducer-embedded compressor plate while the opposite surface was held fixed. The cube was confined on two additional surfaces by lubricated rigid plates to approximate a plane-strain deformation in the scan plane with free slip boundaries. The other two opposing surfaces perpendicular with the scan plan were free to expand under compression.

The 5-cm block was compressed with a motion controller by displacing its top surface downward at a rate of 0.8 mm/s while RF data were acquired from a linear array at 29 frames per second. The first $C = 49$ frames were used for variance estimation. The top surface was displaced 1.35 mm in 1.69 s for a total strain of $\epsilon_T = 0.027$ or 2.7%. The applied strain per frame was $\epsilon_j = 0.055\%$. Displacement variance was found for one-step compression by analyzing echo frames 1 and 49. A two-step multicompression technique summed displacements computed between frames 1 and 25 and frames 25 and 49. Using this method, displacement and strain variances were found by applying 2.7% strain in $C' = 1$, 2, 3, 4, 6 and 8 steps. Frame selection for multicompression estimates with varying number of steps but constant total strain ϵ_T is shown in Fig. 5

Pairs of echo frames with the same relative deformation, e.g., frames (1,49), (2,50),

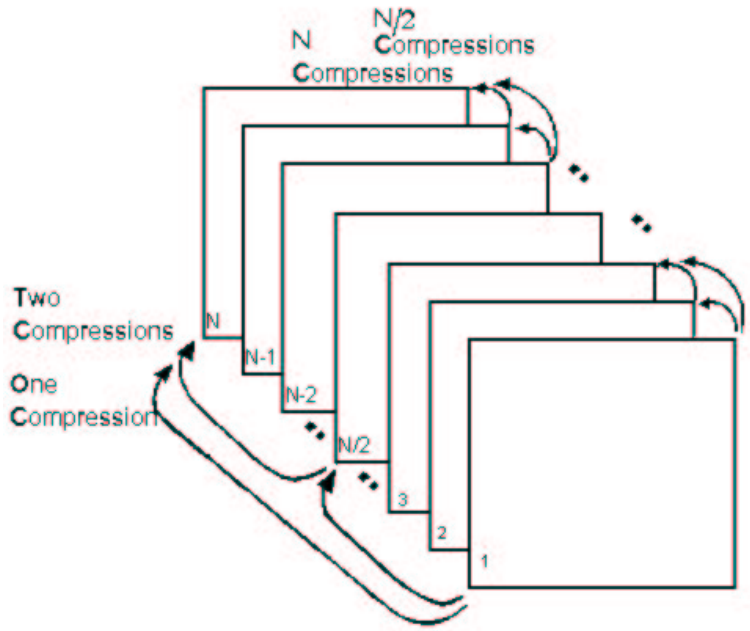

Figure 5. Frame selection for multicompression estimates.

etc., were examined to compute means and standard deviations of the variance estimates; the standard deviations are plotted as error bars in the plots below.

4.2. Displacement estimation.

Displacements are measured using standard 1-D cross correlation techniques. Displacement fields are computed, spatially registered, and summed before calculating the variance. Since the medium is elastically homogeneous and incompressible, spatial registration was accomplished by scaling and translating estimates using global companding techniques.[14] Displacements varied linearly with depth (axial direction), as illustrated in Figure 6(a). We needed to compute the local mean for variance estimation. Therefore we fit the 1-D displacement estimates to a 1st order polynomial

to measure the mean axial displacement field, which is subtracted from the result. But there are still displacement nonstationarities in the lateral direction, so we fit the displacement laterally using a 4th order polynomial that is then subtracted from the estimates. Then we computed the mean square displacement as a variance estimate. Fitting was necessary to eliminate small irregularities, such as gelatin heterogeneities, nonuniform boundary effects, nonstationarities, and shift-varying impulse responses. Fig. 6 (a) is the spatially registered displacement field before subtraction of the mean.

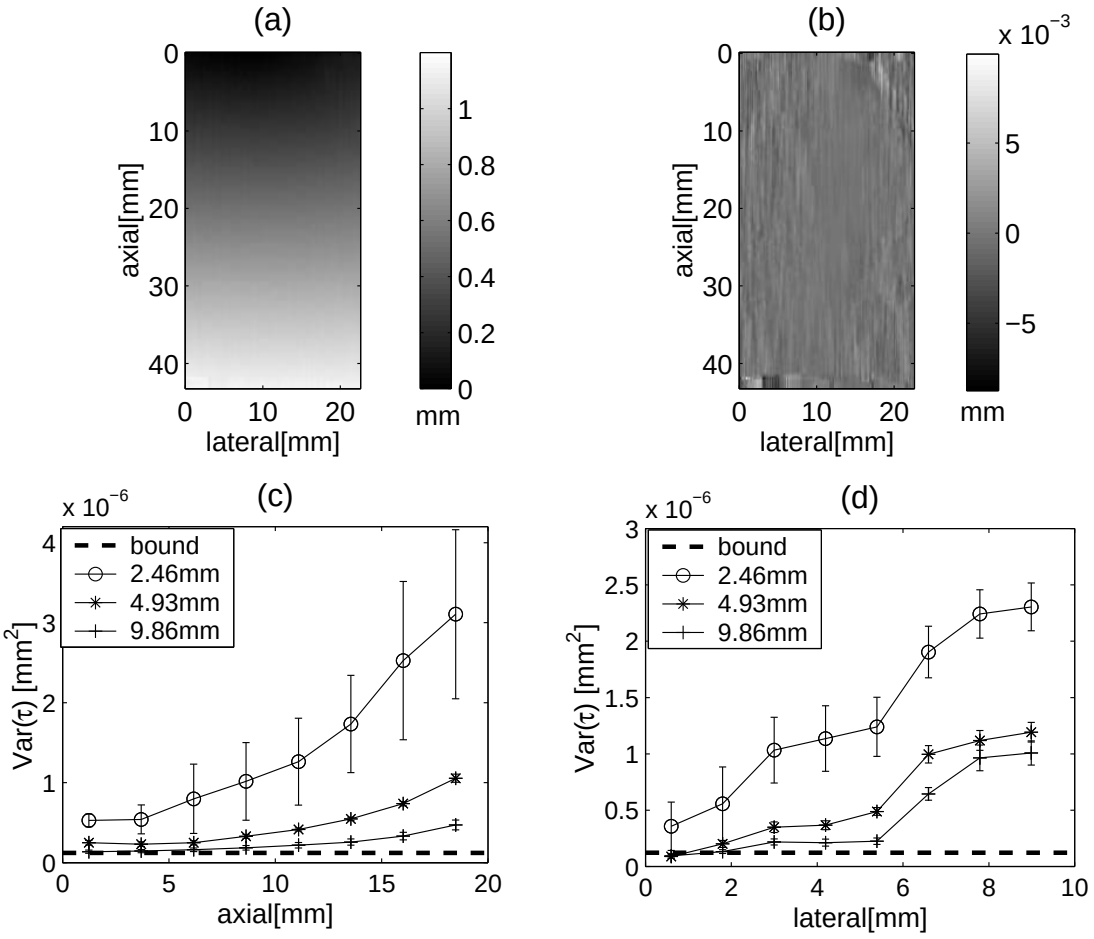

Figure 6. Processing method for displacement variance estimation

(b) is the displacement field of (a) after subtraction of the mean. We chose a rectangular region and centered at the transmission focus for analysis. In (c), the lateral dimension on the field is fixed at 2.4 mm and the axial dimensions (abscissa) varies between 1.2 mm and 18 mm. Results depend of the correlation window size: 2.46 mm, 4.93 mm and 9.86 mm. In (d), the axial dimension is fixed at 5 mm and the lateral dimension is varied between 1.2 mm and 9 mm. Displacement variance was computed from every fourth A-line to minimize correlation between individual estimates. (c) and (d) show that violation of the stationary, shift invariance assumptions lead to increases in variance estimates with field of view compared to the predicted variance bound. We used the data found in Fig. 6 to select an analysis region of 2.4 mm in width (cross range) and 5.0 mm in length (range) with the center at the transmission focus and a correlation window length of 4.93 mm.

4.3. Variance estimation

The sample displacement variance for a C'-step multicompression technique is[35]

$$\begin{aligned}
\mathrm{var}_{C'}(\hat{\tau}) &= \mathrm{var}(\hat{\tau}_1 + \hat{\tau}_2 + \cdots + \hat{\tau}_{C'}) \\
&= E\left\{\left((\hat{\tau}_1 - \bar{\hat{\tau}}_1) + (\hat{\tau}_2 - \bar{\hat{\tau}}_2) + \cdots + (\hat{\tau}_{C'} - \bar{\hat{\tau}}_{C'})\right)^2\right\} \\
&= \sum_{j=1}^{C'} E\left\{(\hat{\tau}_j - \bar{\hat{\tau}}_j)^2\right\} + \sum_{j=1}^{C'} \sum_{j \neq j'} E\left\{(\hat{\tau}_j - \bar{\hat{\tau}}_j)(\hat{\tau}_{j'} - \bar{\hat{\tau}}_{j'})\right\} \\
&= \sum_{j=1}^{C'} \mathrm{var}(\hat{\tau}_j) + \sum_{j=1}^{C'} \sum_{j \neq j'} \mathrm{cov}(\hat{\tau}_j, \hat{\tau}_{j'}) \,, \qquad (36)
\end{aligned}$$

where $1 \leq C' \leq C$ and $\mathrm{cov}(\hat{\tau}_j, \hat{\tau}_{j'})$ is the covariance between the jth and j'th compression steps. If the estimates to be summed are uncorrelated and the compression

steps are equal,

$$\mathrm{var}_{C'}(\hat{\tau}) = C' \,\mathrm{var}(\hat{\tau}_j)\ , \quad \forall j \ \text{ where } \ 1 \leq C' \leq C. \tag{37}$$

For easy understanding, we can use a $C' \times C'$ covariance matrix $\mathbf{O}$ to display the variance and the covariance of the C'-step multicompression. Each element of the matrix $\mathbf{O}_{C' \times C'}$ can be defined as:

$$o_{jj'} = \begin{cases} \mathrm{var}(\hat{\tau}_j) & j = j' \\ \mathrm{cov}(\hat{\tau}_j, \hat{\tau}_{j'}) & j \neq j' \end{cases} \tag{38}$$

The summation of all the elements of the matrix gives the total variance of the C'-step multicompression:

$$\begin{aligned} \mathrm{var}_{C'}(\hat{\tau}) &= \sum_{j=1}^{C'} \sum_{j'=1}^{C'} o_{jj'} \\ &= \sum_{j=1}^{C'} o_{jj} + \sum_{j=1}^{C'} \sum_{j \neq j'} o_{jj'} \end{aligned} \tag{39}$$

Similarly, if all the covariances are zero, the total variance is the summation of the elements on the diagonal of $\mathbf{O}$ as in Eq. 40. Furthermore, if each compression steps are identical, the result is :

$$\mathrm{var}_{C'}(\hat{\tau}) = \sum_{j=1}^{C'} o_{jj} \tag{40}$$

$$= C' o_{jj} \quad \forall j \ \text{ where } \ 1 \leq j \leq C' \tag{41}$$

4.4. Point Spread Function

Measurement of the temporal impulse response, i.e., point spread function (PSF), is an important part of MSC and variance bound computations. The PSF was approximated by scanning a taut human hair ($\sim$0.04 mm diameter) embedded in clear

congealed agar, oriented normal to the beam axis, and positioned 2 cm from a 6.67 MHz linear array near the elevational focus. Digital RF echo data were recorded using the Ultrasound Research Interface (URI) on a Siemens Antares system at 40 Msamples/s (Siemens Medical Systems, Ultrasound Group, Issaquah, WA). The PSF was found by fixing the position of the hair at $\mathbf{x} = \mathbf{x_0}$ and averaging echo samples from twenty data frames to minimize echo noise. The 2-D PSF $h(t[m,n], \mathbf{x_0})$ and the magnitude of its temporal Fourier transform, the system response function $|H(f[k,\ell], \mathbf{x_0})|$, are shown in Figure 7.

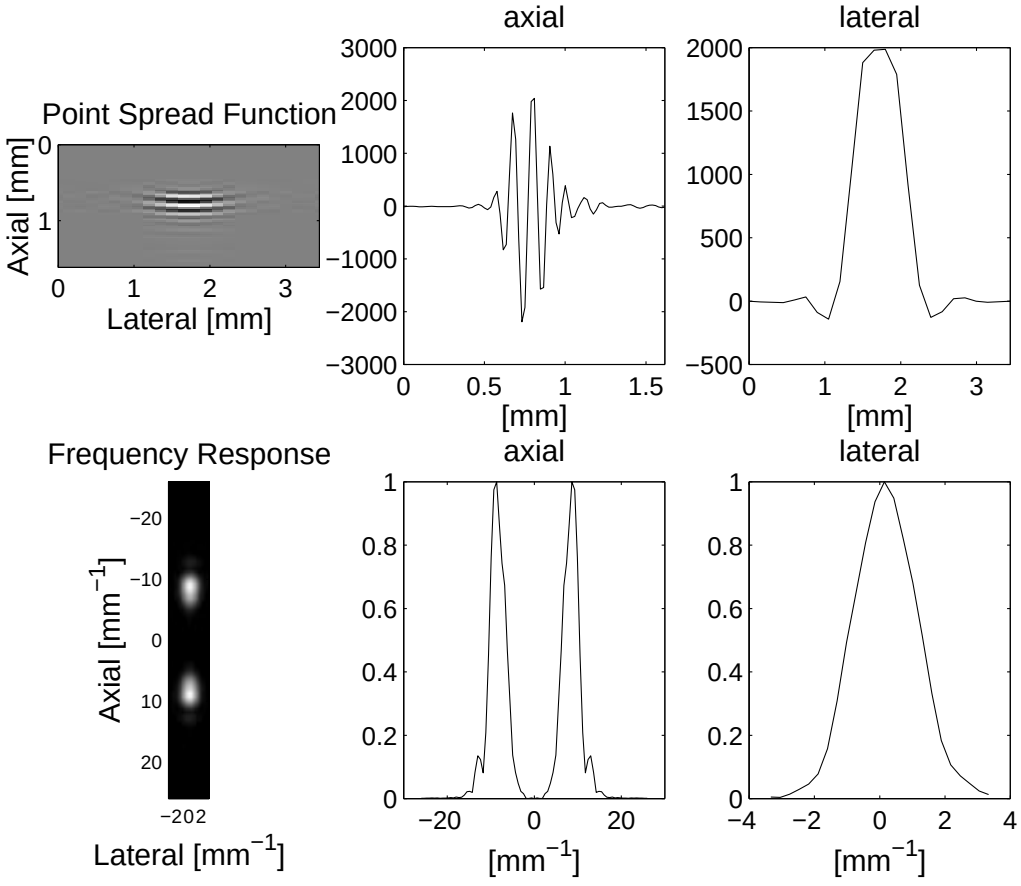

Figure 7. Point spread function.

The top of Fig. 7 represents the point spread function of the linear array and cross sections through the axial and lateral axes. The magnitude of its 2-D Fourier transform is shown at the bottom of the figure. A Gaussian bandpass filter was applied to suppress a small DC value. The hair phantom is a line source rather than a point source of scatter, but the approximation seems reasonable given the results presented in the next section.

A hydrophone was used to scan the transmitted pressure field of the linear array. The elevational focus of the transducer was located at a depth of 2 cm. The in-plane transmit focus was set to 2 cm and all data acquisitions were centered about this range.

4.5. Echo signal-to-noise ratio.

If the random processes are wide-sense stationary and the impulse response is invariant over time and space for all $m, n \in \Omega_i$, then the echo signal-to-noise ratio (eSNR) is given by[36]

$$\text{eSNR} = \frac{\rho}{1-\rho} \; . \tag{42}$$

where ρ is the correlation coefficient. Eq. (42) is derived in the Appendix C for our signal model. Scattering f and noise e functions are assumed to be i.i.d. Gaussian random processes given by, respectively $\mathcal{N}(0, V)$ and $\mathcal{N}(0, 1)$. V is the ratio of variances, $\text{var}(f)/\text{var}(e)$, which can be computed from eSNR and the impulse response:

$$V = \frac{\text{var}(f)}{\text{var}(e)} = \frac{\text{eSNR}}{\int_{-\infty}^{\infty} d\mathbf{x}\; h^2(\mathbf{x}, \mathbf{t}_0)} \; . \tag{43}$$

5. ANALYTICAL AND PHANTOM RESULTS

5.1. Variance Bounds

We used Eq. (33) and Monte Carlo techniques[37] to predict the lower variance bound for displacement variance. From phantom measurements we determined eSNR (43 dB), then we used eSNR along with the PSF to compute the variance ratio, which is found to be $V = 398$. The predicted results are based on an average of 100 trials. For Eq. (33) to hold, we must assume uniaxial compressive strain, Poisson's ratio of $\sim$0.5, and an average displacement of zero; $\mathbf{a} = \mathbf{0}$.

Phantom experimental results are plotted together with predicted values for single compression strain estimation in Fig. 8. Displacement variance is estimated as a function of strain. The correlation window size for experimental data is 4.93mm. We see that the variance changes very little for applied strains less than 0.1%. In this range, electronic noise dominates displacement variance. Above 0.1%, strain induced decorrelation dominates variance. Strains larger than 2% generate very large displacement errors. Since the experiment data match the predictions up to 2%, we find that cross correlators are efficient estimators of displacement.

We selected the largest measured strain in Fig. 8, 2.7%, as the total strain value for the multicompression studies. Eq.36 is used for computing the total variance. Predicted and measured values are plotted in Fig. 9. We found a 78% reduction in displacement variance for a 6-step multicompression technique relative to a single compression technique. Also the lowest variance is found using 6 steps. Error bars

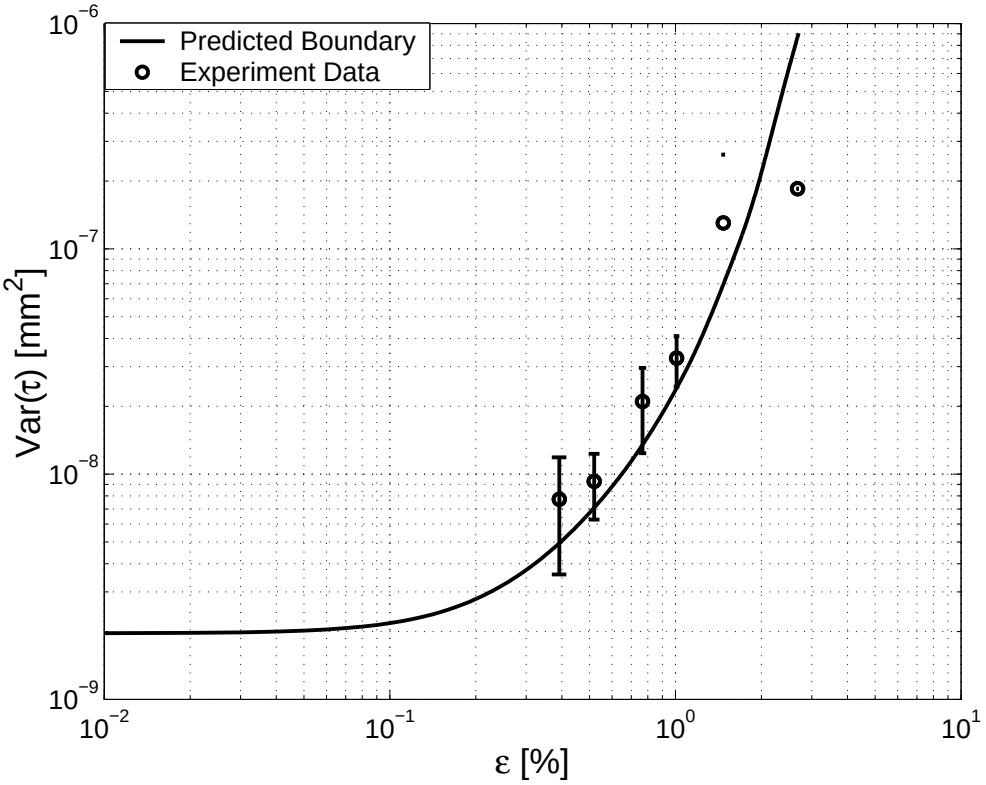

Figure 8. Displacement variance for single compression technique.

in Fig. 8 and 9 indicate one standard deviation. It seems that the predictions break down for strains above 2% in both plots in what we believe is a violation of the small-strain assumption inherent in the Cramér-Rao approach.

5.2. The importance of covariance

In this section, we evaluate the importance of displacement covariance in the estimation of multicompression variance given by Eq. (36). Covariances were included in the data of Fig. 9. These results are reproduced as circles in Fig. 10(a). Assuming between-step covariances are all zero and using Eq. (40), we also plot displacement variance estimates without covariance as crosses in Fig. 10(a). The analysis region

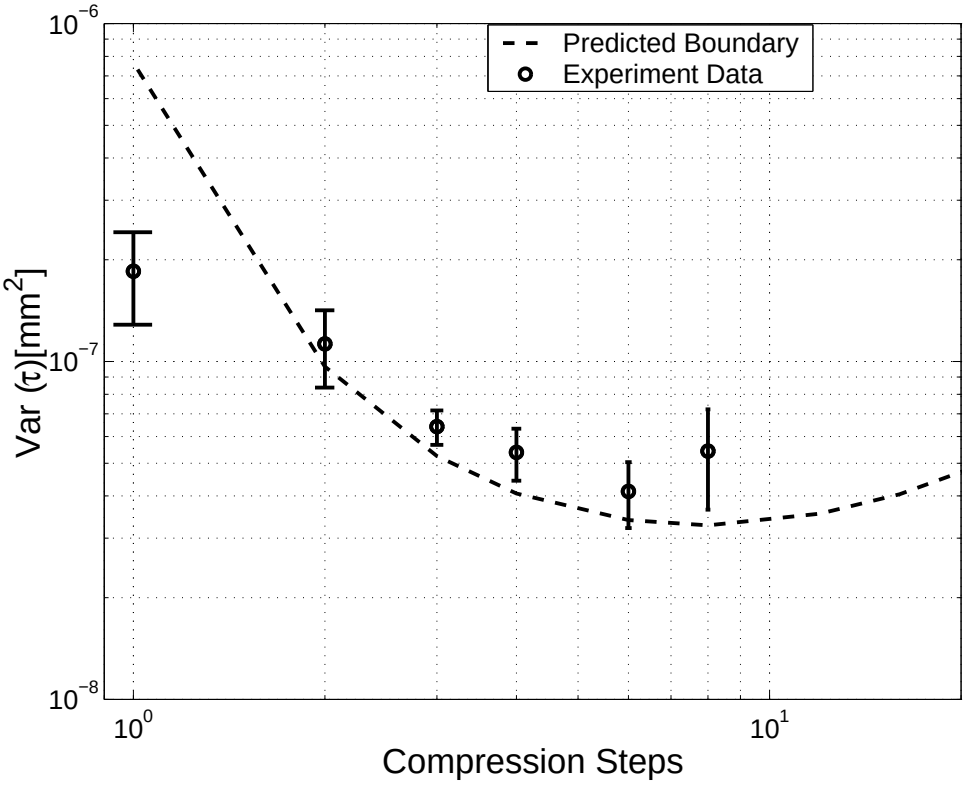

Figure 9. Displacement variance for multicompression technique.

for this phantom data was 2.4 mm × 5.0 mm (range × cross-range) and was centered about the focal length of the transducer. Ignoring the covariances led to an overestimation of the displacement variance. But for this small analysis region, the effect of covariance is relatively small. The 6×6 covariance matrix for the 6-step multicompression technique is shown in Fig. 10(b). The off-diagonal elements of the matrix which indicate covariance between steps are positive and negative.

This analysis was repeated after increasing the region of interest in the phantom to 5.0 mm × 12.3 mm about the focal length; see Figs. 10(c) and (d). We find an order of magnitude increase in both individual variance and covariance terms and the

latter are all positive. When covariances are ignored, the total variance approaches to our predictions. The fact that the variance terms depend on the size of the region of interest despite our efforts to subtract the mean described in Fig. 6 suggests that the nonstationary properties of the medium deformation that interact with a shift-varying system impulse response contribute significantly to displacement errors and ultimately strain noise. We conclude that covariance terms cannot be ignored in Eq. (36) particularly for large regions of interest.

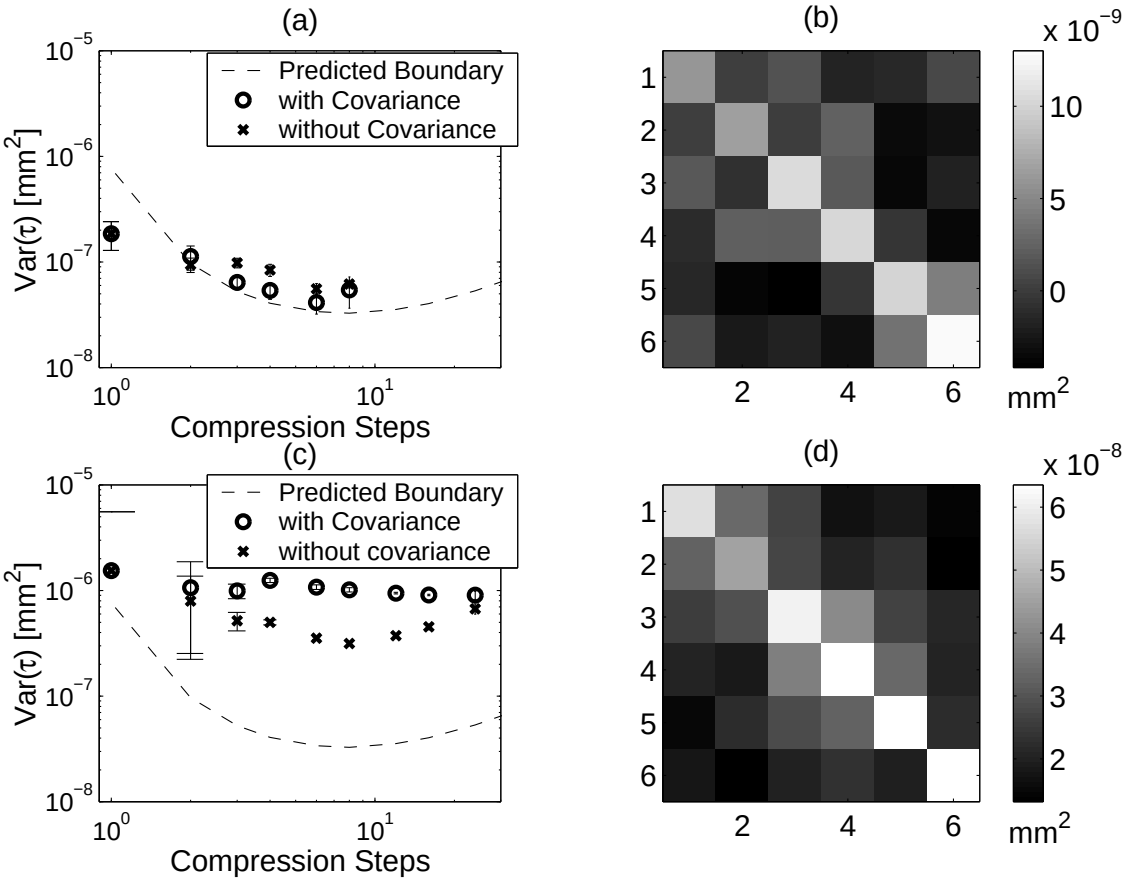

Figure 10. Displacement variance with/without including covariance and the covariance matrix.

5.3. Optimal strain increment

Figs. 8, 9 and 10 validate the analysis and show us situations when the variance bound predicts the measured variance. With this guidance, we now use Eq. (36) and Eq. (37) to design multicompression techniques that yield minimum measurement variance.

We predicted displacement variance bounds by using the 2-D PSF acquired from the Antares system and the gelatin phantom. The instrumentation parameters were the following: 6.67 MHz, 48% bandwidth (-6dB), 0.74mm beam width (-6dB) and eSNR = 43 dB (converted to variance ratio V = 398). If the total strain is less than 0.5%, a single compression strain images have the smallest variance. For $\epsilon_T > 0.5\%$, the concave curves indicate that multicompression techniques can provide smaller displacement variances. The family of curves plotted in Fig. 11 predicts how the displacement variance depends on the number of compression steps when the total compression varies. The optimal number of compressions for each total applied strain value is summarized in Table 2. The data suggest that multicompression techniques can reduce errors when the total applied strain is greater than 0.5%. The number of compression steps that provide minimal variance varies with the total strain, but the strain increment (total applied strain divided by the steps) is always in a certain range of $0.33\% \sim 0.38\%$. The minimum variance occurs when the increment of strain between compressions is approximately 0.35%.

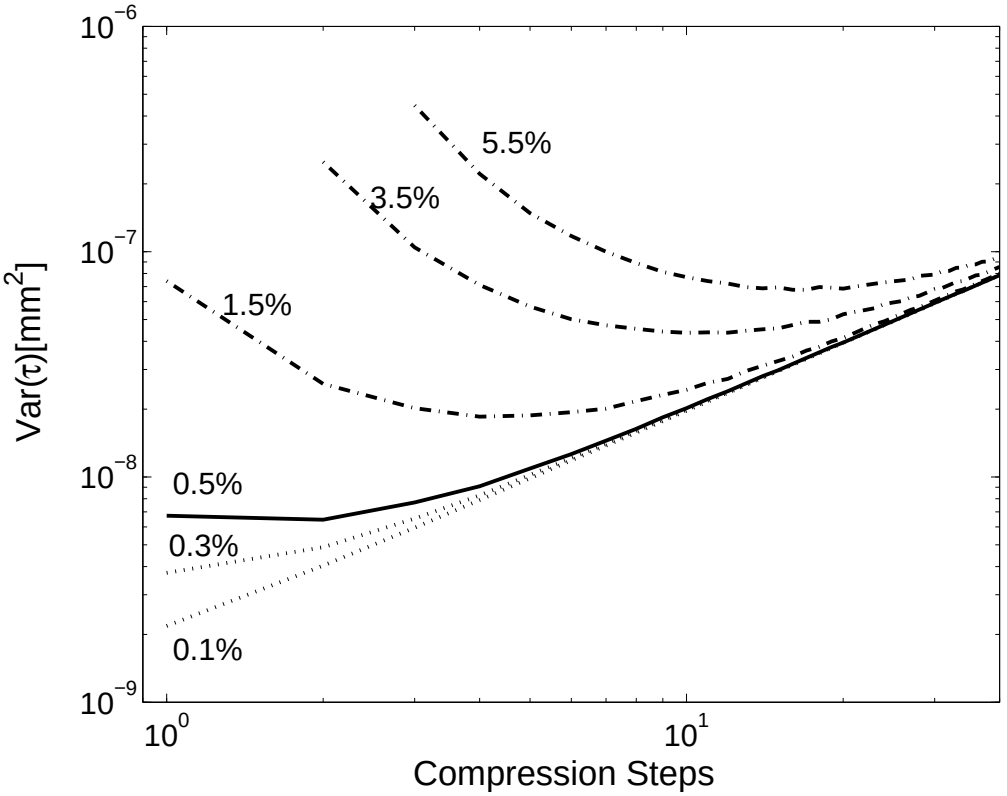

Figure 11. Optimal strain increment estimation.

5.4. Experimental parameters influencing strain errors

The model predicts that echo noise and the system impulse response ultimately limit strain noise. To illustrate this point, strain variances were computed from displacement variances using Eq. (35), where $X = 4.93$ mm and $\Delta X = 0.31$ mm. The strain standard deviation is plotted versus applied strain for single compression techniques where either the variance ratio, bandwidth, or beam width was varied while the other two parameters were held fixed (Fig. 12). The center frequency of a Gaussian frequency spectrum was 5 MHz and the sampling rate was 50 MHz. In Fig. 12 (a) the bandwidth (3.5 MHz or 70% at -6dB) and lateral beam width (0.12 mm at -6dB,

Table 2. Number of steps in multicompression technique that yield minimum displacement variance

Total Strain (%)	Number of Compressions	Strain Increment (%)
0.1	1	0.10
0.2	1	0.20
0.3	1	0.30
0.4	1	0.40
0.5	2	0.25
1.0	3	0.33
1.5	4	0.38
2.5	8	0.31
3.5	12	0.35
4.5	12	0.38
5.5	16	0.34
6.5	19	0.34
7.5	20	0.38

assuming Gaussian aperture) are fixed while varying eSNR. In (b) we fix the variance ratio ($V = 1000$) and beam width (0.12 mm) and vary bandwidths. In (c), the variance ratio ($V = 1000$) and bandwidth (3.5 MHz) are fixed while the beam width is varied.

The variance ratio V (proportional to eSNR if the PSF is known) has the greatest

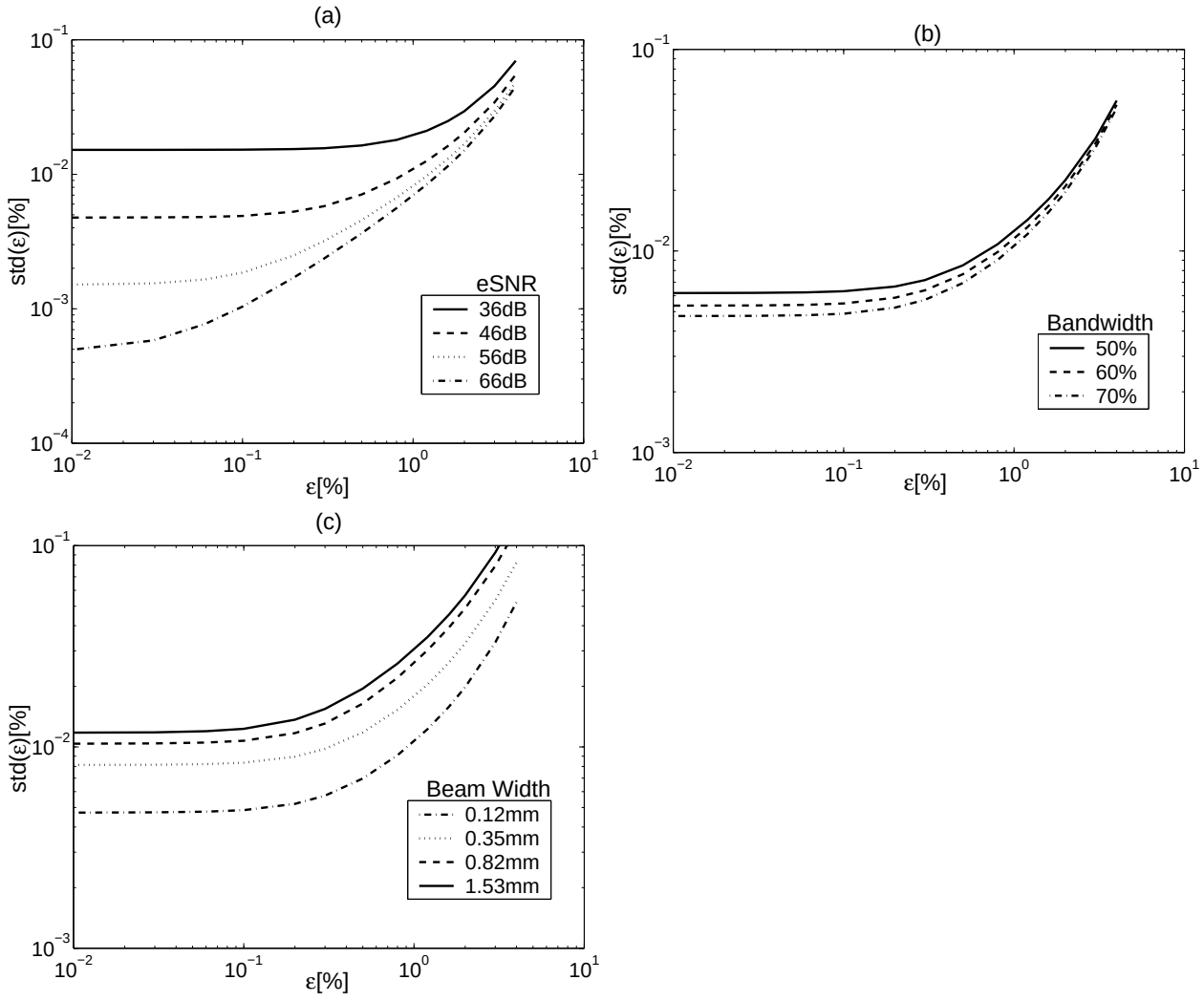

Figure 12. Predicted lower bound for standard deviations of strain estimates.

effect on strain noise particularly at small values of applied strain. At an applied strain of 0.1%, where uncertainty is predominantly from echo noise, Fig. 12(a) shows that increases in eSNR of 10 dB can yield a reduction in variance by as much as an order of magnitude. This effect is not seen at larger values of applied strain, where decorrelation from deformation is the largest source of error.

Figs. 12(b) and (c) show that bandwidth and beam width each affect strain errors

proportionally at all applied strains. Both act on the variance through the system point spread function. Increasing the bandwidth or decreasing the beam width reduces the PSF volume, which reduces the amount of strain on that scale and thus reduces echo decorrelation. These data show that pulse dimensions, normally important for spatial resolution, also significantly influence strain noise.

6. PRELIMINARY CLINICAL EXPERIMENTS

Clinical data using the multicompression techniques are displayed in this section. Compression to the patient breast is applied by freehand with a transducer-embedded compressor plate. We studied totally four cases for in vivo breast imaging.

Three sets of data, two from healthy volunteers and one from a patient with a benign fibroadenoma, were acquired using the Siemens Elegra ultrasound system with a 7.5MHz linear array (7.5L40) transmitting 7.2MHz broadband pulses. RF signals were digitized at 36 Msamples/s, then downsampled by a factor of 2, mixed to form I/Q data and transferred to a PC. Before processing, the data were upsampled by a factor of 4. The strain images were formed from echo data with an effective RF data density of 72 Msamples/s and a bandwidth of 18 MHz. The frame rate is 16 frames per second and the correlation window length is $10.9mm$.

Strain images of two healthy volunteers are shown respectively in Fig. 13 and Fig. 14 with different compression steps. Applying the strain in many small steps clearly reduces noise.

Because of the large compression applied to the breast and the inconsistence of the small compression between each two adjacent frames, only parts of the frames acquired were chosen for calculation. The total compressions was 2% for breast tissue 1 and 4% for breast tissue 2. Normal tissues are relatively homogeneous in strain imaging compared to those with breast lesions, however, even normal breast tissue is elastically heterogeneous.

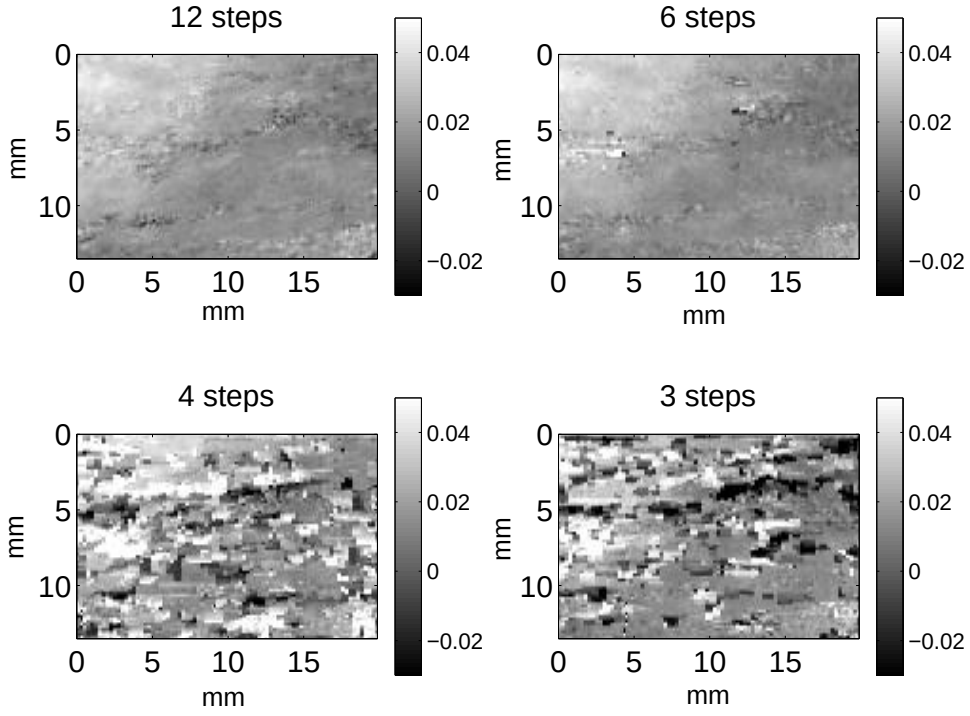

Figure 13. Normal breast tissue 1.

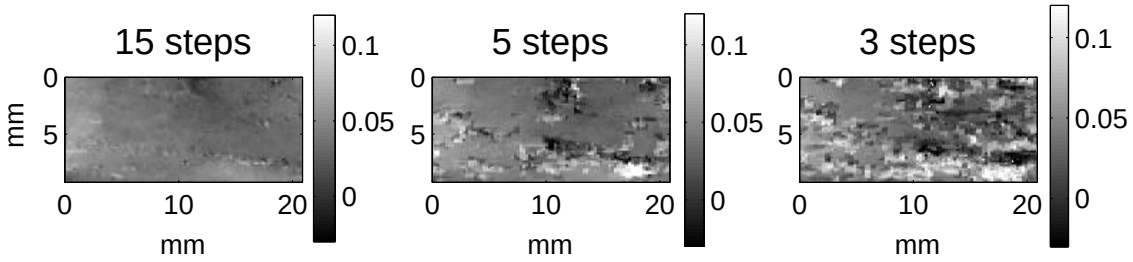

Figure 14. Normal breast tissue 2.

The patient breast with the fibrocystic lesion is compressed 4.7% of its thickness. The 4.7% strain was applied in 36 steps and an ultrasonic echo frame was recorded at each step. Selected images are displayed in Fig.15. When the applied strain per step exceeded 1%, the strain images was entirely filled with decorelation noise (4 steps in Fig.15). At 12 steps (0.39% strain per step) and 18 steps (0.26% strain per step),

the central stiff lesion is clearly seen as a dard region. Increasing the number of steps over 18 appears to reduce lesion contrast.

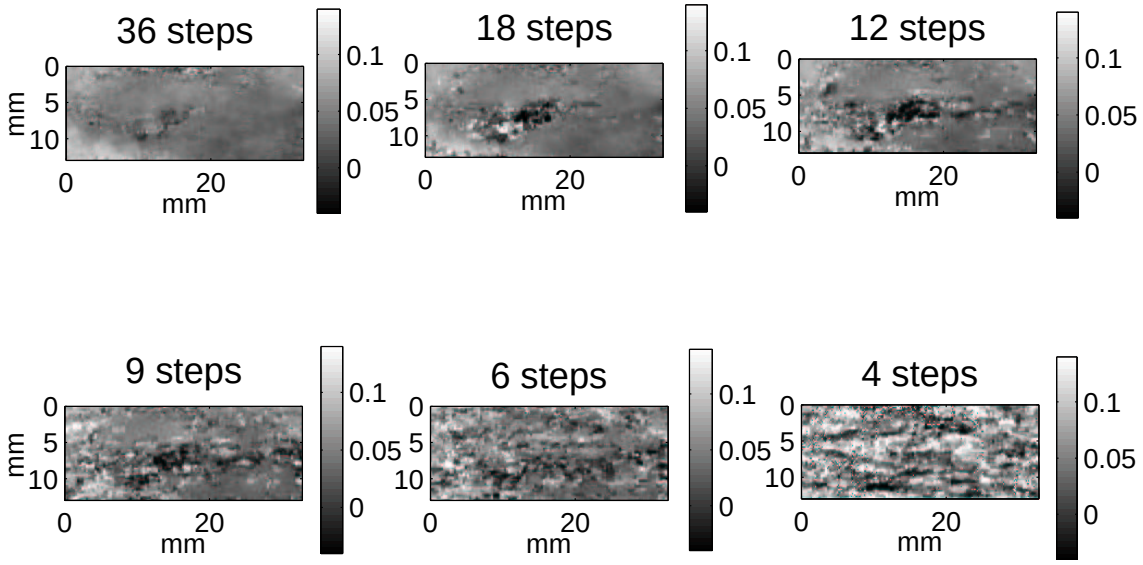

Figure 15. Patient data, images at low frame rate.

One final data set was acquired using the Siemens Antares system with a faster 52 frames per second rate. The total applied compression is only 1.4%. We need a larger decorrelation window length of 19.7mm to smooth images and lower strain noise. The spatial resolution is also reduced. For each set of data, the image with the highest number of compression steps (usually the smoothest one) is regarded as the mean. The mean is subtracted from other images with fewer compression steps, and the standard deviations of the strain are computed and plotted along with the predicted lower bound in Fig.16. The analytical lower bounds are solid lines each having a star to mark the optimal number of steps with the lowest strain noise value; the experimental data are plotted as circles. Fig. 16 (a) and (b) are normal breast

tissue sample 1 and 2. Fig. 16 (c) and (d) are with lesions acquired using low and high frame rate, respectively. The predicted optimal strain increment for homogenous breast imaging is around 0.35% as stated in Chapter 5. When found, the minimum standard deviation for strain in clinical breast images was obtained at approximately one half to one third of the phantom results (0.12% $\sim$ 0.16%). We also note that errors in clinical images far exceed the lower bound.

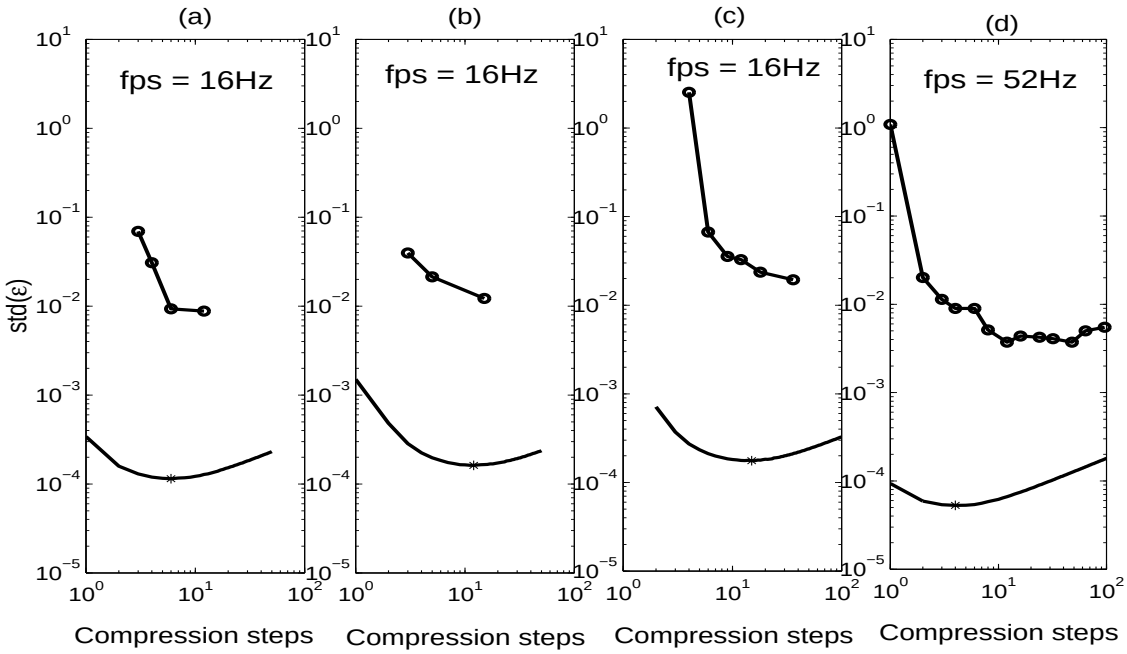

Figure 16. Standard deviation of clinical strain images using multicompression.

Both the images and the curves show the benefits of doing multicompression. Because of the low frame rate, the increasing of the noise at large compression steps which we explained as the accumulation of echo noise are not found in the curves of (a), (b) and (c). In (d), the lowest noise is found at 12 steps multicompression which corresponds to 0.12% increment strain. For a larger number of multicompres-

sion steps, strain noise increases slightly and calculation time for images for motion increases proportionally. For clinical elastography, the greater heterogeneity of breast tissue requires a greater number of small compression steps to obtain minimum noise. The optimal increment strain is in the range of 0.10% to 0.20%.

7. DISCUSSION

When the applied strain is small (<0.1%) and the elastic contrast of structures in the medium is small, displacement estimates are strain independent and limited by echo noise as shown in Fig. 8. For large applied strains (>2%) in the same medium, the large loss of echo coherence dominates estimation errors. Furthermore, the variance bound is not able to predict measured values as assumptions are violated. For $0.1\% \leq \epsilon_T \leq 2\%$, we can rely on Eqs. (33)-(36) to predict the number of compression steps that minimizes strain noise for small homogeneous regions of interest. In one homogenous phantom scanned with a commercial imaging system, eSNR = 43 dB and we found that the minimum strain noise was obtained by limiting the amount of applied strain per compression step to approximately 0.35%. This value also gave what visually appeared to be the lowest noise strain images from in vivo scans where the dynamic range for tissue stiffness was low.[38] In other patients with what appeared to be more heterogeneous breast tissues, the optimal applied strain increment was reduced to 0.15%. The same value was used as the applied strain increment for in vivo breast imaging in previous studies.[39] The strain is much larger in the soft regions of breast tissues that have large stiffness variations, therefore, it is reasonable to expect a lower optimal strain increment for tissues with large dynamic range in stiffness.

The value of 0.35% strain was found for gelatin phantom with the parameters of the Antares system: 6.67 MHz, 48% bandwidth, eSNR = 43 dB, and 0.74 mm

beam width. Others[40] have measured the optimal strain increments in phantoms to be in the range 0.33 – 0.4% via 1-D simulated echo data. For comparison, we entered their system parameters into our analysis: 5.0 MHz, 60% bandwidth (-3 dB) or 85% bandwidth (-6 dB), and eSNR = 40 dB. To convert the analysis into our 2-D equations, we assume an f/2 aperture. Our analysis predicts the optimal strain increment for these parameters to be 0.49%. The difference in results points out the need to carefully consider the dimensionality of the analysis when making predictions.

In conclusion, we found that the optimal strain increment under typical breast imaging conditions is 0.35% if the object contrast of the medium is low, while for relatively heterogenous objects, the optimal strain increment is reduced to about 0.15%. These results were found in phantom data and in vivo breast scans. The optimal strain increment is reduced as the heterogeneity of the tissue increases and as the eSNR increases, suggesting that a large number of small compression steps is recommended for a large dynamic range and in high eSNR conditions. The equations given in this report allow one to predict minimum variance multicompression methods provided that the strain increment is less than 2%.

APPENDIX A. MAXIMUM-LIKELIHOOD STRATEGY

The basic concept of the ML strategy is reviewed in this appendix. Maximum likelihood (ML) method is widely used in signal processing for parameter estimation. Suppose $\mathbf{y} = (\mathbf{y}_1, \mathbf{y}_2, \cdots, \mathbf{y}_n)$ denote n random variables with observation sample data $\mathbf{y}_1 = y_1$, $\mathbf{y}_2 = y_2$, $\cdots$, $\mathbf{y}_n = y_n$. The interest is to estimate an unknown non-random parameter θ based on these data. We assume that the joint probability density function (p.d.f.) of $\mathbf{y}_1, \mathbf{y}_2, \cdots, \mathbf{y}_n$, given by $f_y(y_1, y_2, \cdots, y_n|\theta)$,[35] depends on θ. The main point of estimating θ from the sample data by the ML method is to pick a one-dimensional test statistic $T(\mathbf{y}_1, \mathbf{y}_2, \cdots, \mathbf{y}_n)$ that best evaluate θ in some optimum sense.

The principle of maximum likelihood assumes that the sample data set is representative of the population $f_y(y_1, y_2, \cdots, y_n|\theta)$. Once observation $y_1, y_2, \cdots, y_n$ are given, $f_y(y_1, y_2, \cdots, y_n|\theta)$ is a function of θ alone. Then choose the value for θ that most likely caused the observed data to occur. That means the value of θ that maximizes the above p.d.f. is the most likely value for θ, and it is chosen as its ML estimate $\hat{\theta}_{ML}(\mathbf{y})$.

Given $\mathbf{y}_1 = y_1$, $\mathbf{y}_2 = y_2$, $\cdots$, $\mathbf{y}_n = y_n$, the joint p.d.f. observation $y_1, y_2, \cdots, y_n$ is defined to be the likelihood function, and the ML estimate can be determined from the likelihood equation as[35]:

$$\hat{\theta}_{ML} = \arg\max_{\theta} f_y(y_1, y_2, \cdots, y_n|\theta) \tag{44}$$

or we can use the log-likelihood function:

$$L(y_1, y_2, \cdots, y_n|\theta) = \ln f_y(y_1, y_2, \cdots, y_n|\theta) \tag{45}$$

If $L(y_1, y_2, \cdots, y_n; \theta)$ is differentiable and a maximum $\hat{\theta}_{ML}$ exists, then that must satisfy the equation[35]:

$$\frac{\partial \ln f_y(y_1, y_2, \cdots, y_n; \theta)}{\partial \theta}|_{\theta=\hat{\theta}_{ML}} = 0 \tag{46}$$

APPENDIX B. CRAMÉR-RAO VARIANCE BOUND

Following the notation in the previous section, an estimator $T(\mathbf{y})$ is said to an unbiased estimator for θ if

$$E\{T(\mathbf{y})\} = \theta \tag{47}$$

For all the unbiased estimators of the same parameter, we can find one estimator with the lowest possible variance, which is called Cramér-Rao lower bound. The expression for the Cramér-Rao lower bound is[35]:

$$var\{T(\mathbf{y})\} \geq \frac{1}{E\left\{\left(\frac{\partial}{\partial\theta}\ln f(\mathbf{y}|\theta)\right)^2\right\}} = \frac{-1}{E\left\{\frac{\partial^2}{\partial\theta^2}\ln f(\mathbf{y}|\theta)\right\}} \tag{48}$$

Notice that the Cramér-Rao bound can serve as an approximation to the estimator variance only for unbiased maximum-likelihood estimation.

APPENDIX C. DERIVATION OF ECHO SIGNAL-TO-NOISE RATIO

The following is a derivation of the echo signal-to-noise ratio in terms of a correlation coefficient ρ between a region Ω_i in two echo frames. The result is equivalent to that

found in.[36]

Assume 1-D sequences $g_j[m]$ and $g_{j'}[m]$ are recorded from two echo frames without compressing the object. A time-averaged cross correlation *estimate* $\bar{\hat{\phi}}$ from samples in Ω_i is

$$\bar{\hat{\phi}}_{g_j g_{j'}}[m'] = \frac{1}{M'} \sum_{m \in \Omega_i} g_j[m]\, g_{j'}[m - m'] \; . \tag{49}$$

The time-average correlation *function* is found from the estimate by taking the expected value,

$$\begin{aligned} \bar{\phi}_{g_j g_{j'}}[m'] &= \frac{1}{M'} \sum_{m \in \Omega_i} E\left\{ g_j[m]\, g_{j'}[m - m'] \right\} \\ &= \frac{1}{M'} \sum_{m \in \Omega_i} \phi_{g_j g_{j'}}[m, m - m'] \\ &= \phi_{g_j g_{j'}}[m'] \; , \end{aligned} \tag{50}$$

where the last form is the ergodic property that hold only if the zero-mean object and noise processes are both wide-sense stationary (WSS). Practically, we only have access to Eq. (49). Therefore the correlation coefficient is approximated by

$$\rho \simeq \frac{\bar{\hat{\phi}}_{g_j g_{j'}}[0]}{\sqrt{\left(\bar{\hat{\phi}}_{g_j g_j}[0] \bar{\hat{\phi}}_{g_{j'} g_{j'}}[0] \right)}} \; . \tag{51}$$

Expanding Eq. (50) using Eq. (27) and assuming the impulse response is linear and time invariant over Ω_i, we find

$$\bar{\phi}_{g_j g_{j'}}[m'] = \frac{1}{M'} \sum_{m \in \Omega_i} \int_{-\infty}^{\infty} d\mathbf{x}\, h(mT - 2|\mathbf{x}|/c) \int_{-\infty}^{\infty} d\mathbf{x}'\, h(mT - m'T - 2|\mathbf{x}'|/c)\, E\{ f_j(\mathbf{x}) f_{j'}(\mathbf{x}') \} \; . \tag{52}$$

If the random scattering medium is WSS, then $E\{f_j(\mathbf{x})\, f_{j'}(\mathbf{x}')\} = \mathrm{var}(f)\, \delta(\mathbf{x}-\mathbf{x}')$. Consequently,

$$\begin{aligned} \bar{\phi}_{g_j g_{j'}}[m'] &= \frac{\mathrm{var}(f)}{M'} \sum_{m\in\Omega_i} \int_{-\infty}^{\infty} d\mathbf{x}\, h^2(mT - 2|\mathbf{x}|/c)\ , \\ \bar{\phi}_{g_j g_{j'}}[0] &= \mathrm{var}(f) \int_{-\infty}^{\infty} d\mathbf{x}\, h^2(2|\mathbf{x}|/c)\ , \end{aligned} \tag{53}$$

and

$$\bar{\phi}_{g_j g_j}[0] = \mathrm{var}(f) \int_{-\infty}^{\infty} d\mathbf{x}\, h^2(2|\mathbf{x}|/c) + \mathrm{var}(e) = \bar{\phi}_{g_{j'} g_{j'}}[0]\ . \tag{54}$$

Combining Eqs. (51) - (54), we find the expression for eSNR in Eq. (42). eSNR can only be defined this way for WSS random media where the system impulse response is linear and invariant over space-time. The results are approximate since the noise terms in Eqs. (52) – (54) only cancel completely when temporal averages approach ensemble averages, i.e., Eq (50). Also since eSNR values vary with the scattering source, data from uniformly random phantoms having tissue-like properties and acquired in an isoplanetic region satisfy these assumptions.

REFERENCES

1. M. F. Insana, L. T. Cook, M. Bilgen, P. Chaturvedi, and Y. Zhu, "Maximum-likelihood approach to strain imaging using ultrasound," *J. Acoust. Soc. Am* **107**, pp. 1421–1434, 2000.
2. A. Savazyan, V. Pasechnik, and S. Shnol, "Low speed of sound in gels and biological tissues," *Biofizika* **13**, pp. 587–594, 1968.
3. T. Krouskop, T. Wheeler, F. Kallel, B. Garra, and T. Hall, "Elastic moduli of breast and prostate tissues under compression.," *Ultrasonic Imaging* **20**, p. 260, 1998.
4. S. Goss, R. Johnston, and F. Dunn, "Comprehensive comilation of empirical ultrasonic properties of mammalian tissues," *J. Acoust. Soc. Amer.* **64**, pp. 423–457, 1978.
5. R. Lerner, K. P. J. Holen, R. Gramiak, and R. Waag, "Sonoelasticity:medical elasticity images derived from ultrsound signals in mechanicall vibrated targets," *Acoust. Imaging* **16**, pp. 317–327, 1988.
6. Y. Yamakoshi, J. Sato, and T. Sato, "Ultrasonic imaging of internal vibration of soft tissue under forced vibration," *IEEE Trans Ultrason Ferroelectr Freq Control* **37**, pp. 45–53, 1990.
7. J. Ophir, I. Céspedes, H. Ponnekanti, Y. Yazdi, and X. Li, "Elastography: a qualititve method for imaging the elasticity of the biological tissues," *Ultrasonic Imaging* **13**, pp. 111–134, 1991.
8. J. Greenleaf, M. Fatemi, and M. Insana, "Selected methods for imaging elastic properties of biological tissues," *Annu. Rev. Biomed. Eng.* **5**, pp. 57–78, 2003.
9. B. Garra, E. Céspedes, J. Ophir, S. Spratt, R. Zuurbier, C. Magnant, and M. Pennanen, "Elastography of breast lesions: initial clinical results," *Radiology* **202**, pp. 79–86, 1997.
10. T. Hall, Y. Zhu, and C. Spalding, "In vivo real-time freehand palpation imaging," *Ultrasound Med. Biol.* **29**, pp. 427–435, 2003.
11. A. Hoeks, P. Brands, J. Willigers, and R. Reneman, "Non-invasive measurement of mechanical properties of arteries in health and disease," *Proc. Instn. Mech. Engrs.* **213**, pp. 195–202, 1999.
12. J. K. Tsou, J. J. Mai, F. A. Lupotti, and M. F. Insana, "Simultaneous narrow-band ultrasonic strain-flow imaging," *Proc. SPIE* **5373**, pp. 173–83, 2004.

13. K. Nightingale, M. Soo, R. Nightingale, and G. Trahey, "Acoustic radiation force impulse imaging: in vivo demonstration of clinical feasibility," *Ultrasound Med. Biol.* **28**, pp. 227–235, 2002.

14. P. Chaturvedi, M. Insana, and T. Hall, "2-D companding for noise reduction in strain imagin," *IEEE Trans. Ultrason., Ferro., Freq. Contrl.* **45**, pp. 179–191, 1998.

15. Y. Fung, *Biomechanics: Mechanical Properties of Living Tissues*, Springer-Verlag, New York, 1993.

16. *http://www.cancer.org*, American and Cancer and Society (ACS).

17. M. O'Donnell, A. Skovorada, B. Shapo, and S. Emelianov, "Internal displacement and strain imaging using ultrasonic speckle tracking.," *IEEE Trans. Ultrason. Ferro. Freq. Contrl.* **41**, pp. 314–325, 1994.

18. A. Skovorada, S. Emelianov, M. Lubinski, A. Sarvazyan, and M. O'Donnell, "Theoretical analysis and verification of ultrasound displacement and strain imaging.," *IEEE Trans. Ultrason. Ferro. Freq. Contrl.* **41**, pp. 302–313, 1994.

19. T. Varghese and J. Ophir, "A theoretical frame work for performance characterization of elastography: the strain filter," *IEEE Tran. Ultrason. Ferroelec. Freq. Control.* **44**, pp. 164–172, 1997.

20. T. Varghese, J.Ophir, and I. Cespedes, "Noise reduction in elastograms using temporal stretching with multicompression averaging," *Ultrasound Med. Biol.* **22**, pp. 1043–1052, 1996.

21. A. Pesavento, A. Lorenz, H. Ermert, H. Sommerfeld, M. Garcia-Schúrmann, T. Senge, and S. Philippou, "Frame-to-frame statistics of real-time strain images," *IEEE Ultrasonics Symposium* **2**, pp. 1809–1812, 2000.

22. M. Bilgen and M. Insana, "Covariance analysis of time delay estimates for strained signals," *IEEE Tran. Sig. Proc.* **46**, pp. 2589–2600, 1998.

23. G. Carter, *Coherence and Time Delay Estimation*, IEEE Press, Piscataway, NJ, 1993.

24. R. Maurice and M. Bertrand, "Lagrangian speckle model and tissue-motion estimation-theory [ultrasonography]," *IEEE Trans. Med. Imaging* **18**, pp. 593–603, 1999.

25. F. Kallel and M. Bertrand, "Speckle motion artifact under tissue rotation," *IEEE Trans. Ultrason. Ferroelectr. Freq. Control* **41**, pp. 105–122, 1994.

26. C. Knapp and G. Carter, "Estimation of time delay in the presence of source or receiver motion," *J. Acoust. Soc. Am* **61**, pp. 1545–1549, 1977.

27. Y. Zhu, P. Chaturvedi, and M. Insana, "Strain imaging with a deformable mesh," *Ultrason. Imaging* **21**, pp. 127–141, 1999.

28. G. Carter, C. Knapp, and A. Nuttall, "Estimation of the magnitude-squared coherence function via overlapped fast fourier transform processing," *IEEE Trans. Audio Electroacoust.* **21**, pp. 337–344, 1973.

29. C. Knapp and G. Carter, "The generalized correlation method for estimation of time delay," *IEEE Trans. Acoust., Speech, Signal. Process.* **24**, pp. 320–327, 1976.

30. S. Kay, *Fundamentals of Statistical Signal Processing: Estimation Theory*, PTR Prentice Hall, Englewood Cliffs, NJ, 1993.

31. J. Melsa and D. Cohn, *Decision and Estimation Theory*, McGraw-Hill, New York, 1978.

32. R. Zemp, C. Abbey, and M. Insana, "Linear system models for ultrasonic imaging: application to signal statistics," *IEEE Trans. Ultrason. Ferro. Freq. Contrl.* **50**, pp. 642–654, 2003.

33. I. Cespedes, M. F. Insana, and J. Ophir, "Theoretical bounds on strain estimation in elastography," *IEEE Trans. Ultrason., Ferro., Freq. Contrl.* **42**, pp. 969–972, 1995.

34. T. Hall, M. Bilgen, M. Insana, and T. Krouskop, "Phantom materials for elastography," *IEEE Trans. Ultrason., Ferro., Freq. Contrl.* **44**, pp. 1355–1365, 1997.

35. A. Papoulis and S. Pillai, *Probability, Random Variables and Stochastic Processes*, McGraw-Hill, Boston, MA, 2002.

36. I. Cespedes, J. Ophir, and S. Alam, "The combined effect of signal decorrelation and random noise on the variance of time delay estimation.," *IEEE Trans. Ultrason., Ferro., Freq. Contrl.* **44**, pp. 220–225, 1997.

37. J. Liu, C. Abbey, and M. Insana, "Linear approach to axial resolution in elaticity imaging," *IEEE Trans. Ultrason. Ferro. Freq. Contrl.* **51**, pp. 716–725, 2004.

38. C. Pellot-Barakat, F. Frouin, M. F. Insana, and A. Herment, "Ultrasound elstography based on multi-scale estimations of regularized displacement fields," *IEEE Trans. Med. Imaging* **23**, pp. 153–163, 2004.

39. C. Pellot-Barakat, F. Frouin, A. Herment, J. Mai, K. Lindfors, J. Tsou, P. V. Behren, and M. F. Insana, "A regularized approach for freehand ultrasound elastography of breast lesions," *IEEE ISBI* , pp. 952–955, 2004.

40. T. Varghese and J. Ophir, "Performance optimization in elastography: Multicompression with temporal stretching," *Ultrasonic Imaging* **18**, pp. 193–214, 1996.